Geology and mineralization of the Cu-rich Mumbwa district, a potential IOCG-type system at the eastern margin of the Pan-African Hook batholith, Zambia

Lorenzo Milani [a,b], Jérémie Lehmann [b,c], Kalin V. Naydenov [b,d], Kerstin Saalmann [e], Paul A.M. Nex [b], Judith A. Kinnaird [b], Ira S. Friedman [f], Thomas Woolrych [g], David Selley [h]

[a] Department of Geology, University of Pretoria, PVT Bag X20, Hatfield 0028, Pretoria, South Africa.
[b] School of Geosciences, University of the Witwatersrand, PVT Bag 3, Wits, 2050, Johannesburg, South Africa.
[c] Department of Geology, University of Johannesburg, PO Box 524, Auckland Park 2006, Kingsway & University (APK campus), Johannesburg, South Africa.
[d] Geological Institute; Bulgarian Academy of Sciences; Acad. G. Bonchev str., bl. 24, 1113 Sofia, Bulgaria.
[e] Geological Survey of Norway (NGU), Postboks 6315 Sluppen, 7491 Trondheim, Norway.
[f] Anglo American, 11 Katemo Road, Rhodes Park, Lusaka, Zambia.
[g] Intrepid Mines Limited, 78- 80 William Street, Woolloomooloo NSW 2011, Australia.
[h] Sandy Bay Campus, Geography-Geology Building, University of Tasmania, PVT Bag 79, Hobart Tasmania 7001, Australia.

Corresponding author: Lorenzo Milani - Department of Geology, University of Pretoria, PVT Bag X20, Hatfield 0028, Pretoria, South Africa. E-mail address: lorenzgugl@gmail.com

Abstract

The Mumbwa mineralized district is located approximately 200 km west of Lusaka, at the north-eastern margin of the Pan-African granitic Hook batholith. Polymetallic sulphide occurrences in the area have been known for hundreds of years, but more recent geophysical and geochemical investigations led to the discovery of a copper-rich hydrothermal system, mostly associated with late-stage syenite intrusions of the Hook batholith. The extent of the hydrothermal system is not known, but to date two main centres have been identified, the Sugar Loaf and Mutoya.

Sulphide mineralization occurs along regional-scale lineaments, following a 25 km-long NNW-trending corridor. Mineralized host rocks are characterized by brecciation, often pervasively replaced by magnetite-hematite, and by strong metasomatism with multiple - and often superimposed - alteration cycles, from potassic, to carbonate, sericite-chlorite and

amphibole-apatite-carbonate. Sulphur isotopes suggest that a mixture of magmatic and sedimentary-derived evaporitic fluids were critical in providing sulphur and metals. Late syenitic intrusions triggered the relevant hydrothermal circulation and favoured the mineralization processes.
Diagrams plotting key element geochemistry and alteration indexes highlight vectors to alteration and mineralization and suggest that the sulphides preferably concentrated in rocks affected by hydrothermal iron oxides in association with sericite-chlorite alteration.
At the Kitumba prospect (in the Sugar Loaf mineralized centre), granitic to syenitic bodies host a hypogene copper mineralization (mostly chalcopyrite), that was subsequently overprinted by pervasive and deep supergene mineralization (malachite, chalcocite, chalcosiderite, cuprite, digenite, chrysocolla, bornite, native copper). Supergene mineralization has been identified in boreholes to depths exceeding 700 m. Reserves at Kitumba are estimated at 27.9 Mt with an average grade of 2.2% copper at a 1.0% copper cut-off grade. Gold is present, although generally at low grades.
In the Mutoya centre, metasedimentary rocks alternate with felsic intrusions. Two prospects have been identified, characterized by large areas of magnetite-hematite breccias hosting sulphide mineralization with predominantly pyrite and minor chalcopyrite.
An affiliation to the iron oxide copper gold (IOCG) category is discussed. Many, but not all of the distinctive IOCG features, are present in the studied area.

1. Introduction

The Mumbwa district, in Central Zambia (Fig. 1), represents an interesting example of a Cambrian orogenic mineralized system, with copper (± gold) mineralization associated with hydrothermal iron oxides, breccias and veins (Cikin and Drysdall, 1971; Robertson, 2013). The district, which is located along the north-eastern margin of the syn-tectonic Pan-African Hook batholith, is hosted by Neoproterozoic to early Paleozoic metasedimentary rocks of the Katanga Supergroup in the vicinity of late-tectonic syenite plutons (Abell, 1970, 1976; Cikin and Drysdall, 1971; Page, 1974; Pipping, 1975, Hanson et al., 1993; Griffiths, 1998; Naydenov et al., 2016).
The area has been known for its copper potential for hundreds of years (Cikin and Drysdall, 1971; Robertson, 2013). The first commercial copper mines in Zambia at Sable Antelope (Fig. 2) and Hippo (approximately 30 km NW of the studied area, beyond Fig. 2), date back to 1897 and mark the beginning of the industrial era for copper in Zambia. The mining rush between 1906 and 1923 led to the discovery of several other base metal occurrences throughout an area soon known as ‘The Big Concession’ (Cikin and Drysdall, 1971), with copper as the main commodity, occurring in mineralized sideritic breccias, in oxidized

deposits in shales and metasandstones, and in association with syenitic rocks. Historical copper mines are Silver King, Crystal Jacket, Sable Antelope, Blue Jacket, True Blue, Kamiyobo, Lou Lou, Sugar Loaf/Copper Queen (Fig. 2), and Maurice Gifford and North Star (outside Fig. 2). In addition to copper, non-economic zinc silicates, iron enrichments and minor gold and silver occurrences have occasionally been described (Cikin and Drysdall, 1971).

With the discovery of the Zambian Copperbelt to the north, little activity occurred in the region until the 1990s, when Billiton acquired new ground geophysical and geochemical data, which led to the discovery of a series of Cu-Au anomalies spatially associated with alteration or brecciation zones, and interpreted as part of a large-scale hydrothermal-mineralized system (Waller et al., 2014).

In 2004, a geophysical survey cantered on the Mumbwa district was commissioned by a joint venture between BHP Billiton and Blackthorn Resources (AIM Resources, Dransfield and Christensen, 2013; Woolrych et al., 2015; Fig. 3). Twenty-seven potential targets were identified by integrating geophysics with soil geochemistry. Several targets are aligned along a ~ NNW-SSE-striking structural corridor defined by the Mumbwa Fault Zone and the Kitumba Fault Zone (Fig. 2), and are characterized by massive magnetite or hematite replacement of intrusive and metasedimentary rocks (Robertson, 2013; Waller et al., 2014). Two areas, separated by the ENE-striking Kankamu Fault (Fig. 2), enclose the most promising prospects, and are here referred as the Sugar Loaf (named after the historical mine) and Mutoya centres.

The Sugar Loaf centre comprises a series of intrusive bodies that are granitic to syenitic in composition. The interest in the area rapidly focused on the Kitumba porphyritic syenite prospect, and, when in 2014 Blackthorn Resources merged with Intrepid Mines Ltd, the venture was granted a large-scale mining license for the development and operation of the Kitumba prospect, with pre-feasibility studies, including a number of mining options and production rates completed (Waller et al., 2014). Using a 1% Cu cut-off grade, total Measured and Indicated Mineral Resource were estimated at 27.9 Mt at 2.2% Cu for a total of ~ 500,000 tons of contained copper (Intrepid Mines Ltd Annual Report, 2017). Gold, with an average grade of 0.03-0.04 g/t, is locally elevated but sub-economic.

Potential exists for further copper mineralization close to the Kitumba prospect, especially at the intersections between the Mumbwa Fault Zone and the ENE-striking Kankamu Fault. In the recently outlined satellite Kakozhi prospect, 5 km NW of Kitumba (Fig. 2, 4), exploration has defined a mineralized system lithologically similar to Kitumba, with quartz-feldspar porphyry granite and fine-grained syenite intruding Kundelungu metasedimentary rocks (Robertson, 2013; Waller et al., 2014). The intrusions at Kakozhi appear undeformed and only locally brecciated. Pervasive iron oxide alteration as well as hematite, specularite and

magnetite veining variably affect the magmatic and metasedimentary rocks. Preliminary drilling revealed zones of leaching and/or reconcentration of copper, as defined by low-grade copper intersections associated with the upper oxidized and ferruginized parts of the drillholes.

The Mutoya centre consists of an intrusive body in contact with a metasedimentary sequence to the south, and a manganosiderite-altered zone to the north (the latter originally known as 'the Worm'). Two main prospects: Mutoya s.s. (*sensu stricto*) to the south, and Mushingashi to the north, have been outlined (Fig. 2). Encouraging copper anomalies were intersected during preliminary drilling. Further investigations were concentrated at the transition between magnetite-rich and hematite-rich zones, which appear to be the most favourable zone for precipitation of copper sulphides with an estimated grade of ~ 0.1% Cu (P.L. Mann, pers. comm., 2011). With the main interest for exploration concentrating at Kitumba, the activity at the Mutoya centre was temporally suspended. At the moment a detailed geological map of the Mutoya area cannot be traced and the relatively limited drilling makes drawing of cross-sections problematic. Lack of information also prevents an evaluation of the potential and spatial extent of the mineralization-alteration system. Nevertheless, this paper focuses on both centres, and provides the first study on the ore deposit potential of the district. It contains a synthesis of information collected during early exploration stages that has been combined with new data. Processing of aeromagnetic data suggests that the late-stage syenite bodies, spatially associated with the mineralization, extend over a larger area than previously thought. Macro- and microscopic observations on core samples provide an opportunity to study mineralization and alteration styles of the main mineralized centres of Sugar Loaf and Mutoya. Sulphur isotope data on sulphides imply a combination of possible sources of metals and sulphur. Major and trace element geochemistry acquired on representative rocks enables a comparison between inferred protoliths and altered samples to be made, thus constraining possible vectors to alteration and mineralization. An affinity with IOCG systems, in particular at Kitumba, is justified by the close association of copper and subordinate gold mineralization to a large-scale iron oxide alteration system, where oxidation and ore developed along faults and fault splays, intersections, and dilational jogs.

2. Geological setting

2.1. Regional geology

The Mumbwa district is located at the north-eastern margin of the Pan-African Hook granitic batholith (Cikin and Drysdall, 1971; Robertson, 2013; Waller et al., 2014), which extends

over 12,000 sq. km approximately 200 km west of Lusaka, in Central Zambia. The batholith is related to the development of the Damara-Lufilian-Zambezi orogenic system, which formed during the assembly of the Gondwana supercontinent as a result of the collision between the Congo and Kalahari cratons (e.g., Gray et al., 2008; Miller, 2008; Frimmel et al., 2011, Fig. 1A). It is in fact inferred that the Damara belt of Namibia extends under cover into Botswana, joining to the east with the Lufilian Arc and the Zambezi, Mozambique and Lurio belts (Goscombe et al. 2000; Hanson 2003). In Zambia, the orogenic system developed in two main branches: the arcuate fold and thrust belt of the Lufilian Arc in the north and the E-W-trending Zambezi belt to the south (Fig. 1B).

The Lufilian Arc comprises a predominantly metasedimentary siliciclastic, carbonate, and evaporitic sequence of Neoproterozoic to Cambrian age (Katanga Supergroup, Unrug, 1988; Kampunzu et al., 2000; Porada and Berhorst, 2000). The Katanga Supergroup rocks were deformed and metamorphosed during the Pan-African orogeny at ~ 540 and ~ 512, Ma with peak greenschist facies conditions at ~ 530-520 Ma, followed by exhumation and cooling until ~ 480 Ma (Porada and Berhorst, 2000; John et al., 2003, 2004a; Rainaud et al., 2005). To the south of the main structural system of the Mwembeshi Zone, the Zambezi belt (Fig. 1B) is represented by clastic and carbonate rocks overlying a thick package of metarhyolites and metabasalts of the Zambezi Supracrustal sequence (Hanson et al., 1994; Johnson et al., 2007). The Zambezi Supracrustal sequence is interpreted to be the southern extension of the Katanga Supergroup (Annels, 1974; Unrug 1988; Porada 1989; Binda 1994; Porada and Berhorst 2000; Johnson et al. 2005, 2007). Within the Zambezi belt, fragments of MORB-type mafic rocks, metamorphosed to eclogite facies, mark the cratonic suture (Vrána et al., 1975; John and Schenk, 2003; John et al., 2003, 2004b; Johnson et al., 2007). Geochronological constraints indicate that the subduction was active between 650-600 Ma (John et al., 2004a, b) and was followed by collision at ~ 530 Ma (Naydenov et al., 2014, 2016), the latter having been responsible for upper-greenschist to mid-amphibolite facies metamorphism of the Zambezi Supracrustal sequence (Hanson et al., 1994; Hargrove et al., 2003).

2.2. Local geology: Hook batholith and Katanga Supergroup metasedimentary rocks

The geology of the Hook batholith, situated at the junction between the inner part of the Lufilian Arc and the western end of the Zambezi belt, has recently been reviewed (Naydenov et al., 2014; Milani et al., 2015). The batholith is predominantly felsic and classified as A-type, metaluminous and alkali-calcic to alkaline. It is locally highly gneissified and mylonitized. The main lithologies include fine- to medium-grained biotite granites, coarse-grained and megacrystic biotite granites, leucocratic and tourmaline-bearing granites, and

post-tectonic satellite intrusions mainly syenitic in composition. The syenites straddle the eastern margin of the batholith (Fig. 1C) and texturally range from aphanitic to feldspar- or quartz-porphyritic. They are undeformed and in the Mumbwa district they are often spatially associated with pervasive alteration and hydrothermal mineralization (Cikin, 1972; Hanson et al., 1993).

Recent U-Pb zircon ages on granitoids constrain the age of the batholith between 550 and 540 Ma (Naydenov et al., 2014; Milani et al., 2015), with an unpublished U-Pb zircon age at 522 ± 3 for a syenite type rock at the Kitumba prospect (P.L. Mann, pers. comm., 2011). This age confirms that the syenites represent the final pulses of the Hook batholith, although caution has to be adopted given the metamictization of the dated zircons. Small outcrops of mafic rocks, mainly gabbro to gabbrodiorite in composition, have been documented in the easternmost part of the Hook Batholith. U-Pb zircon ages, between 570 and 520 Ma, indicate that the mafic intrusions were partly coeval with the main batholith (Milani et al., 2015).

The northern, western and southern margins of the Hook batholith are covered by rocks of the Karoo Supergroup and Kalahari Group so that the extent of the batholith is unknown (Fig. 1C). The eastern margin of the batholith is in contact with rocks belonging to the Katanga Supergroup, represented by a metasedimentary succession (upper greenschist facies) of quartzites and fine-grained quartzite-sericite schists overlain by dolomites, marbles, calc-silicates and schists. A correlation of this succession with the lower and middle Kundelungu Group of the Copperbelt stratigraphy has been proposed (Phillips and Newton, 1956; Phillips, 1965; Abell, 1970; Cikin and Drysdall, 1971; Vajner, 1998). This sequence is overlain unconformably by an arenaceous and argillaceous succession that is locally conglomeratic and metamorphosed to greenschist facies (upper Kundelungu Group, de Swardt and Drysdall, 1964). The conglomerate includes pebbles from the underlying metasedimentary formations as well as detrital zircons of Hook batholith age (Naydenov et al., 2014), thus indicating a major unconformity and sedimentation after the exhumation of the Hook batholith (de Swardt and Drysdall, 1964). The age of the Katanga Supergroup in this area remains poorly constrained.

The emplacement of the Hook batholith during E-W regional shortening (D1, 550-533 Ma) resulted in folded metasedimentary rocks to the east and NE of the batholith at lower greenschist facies conditions (Naydenov et al., 2014). A second deformation event (D2, ≤ 530 Ma) occurred during a N-S regional shortening that overprinted and refolded the D1 fabrics in the eastern part of the batholith (Naydenov et al., 2016). Along the Mwembeshi Zone, siliciclastic metasedimentary rocks containing detrital zircons of Hook batholith age record only the D2 deformation, and are therefore considered syn-to post-tectonic to the exhumation of the batholith (molasse-type deposits, Naydenov et al., 2014).

2.3. Mineralization

In the studied area, primary copper mineralization is commonly characterized by disseminated to semi-massive chalcopyrite (± bornite) associated with diffuse magnetite/hematite oxidation and brecciation. Part of the district has been affected by strong weathering, resulting in a diffused supergene mineralization comprising native copper, malachite, chalcocite, copper phosphate, cuprite, covellite, digenite, chrysocolla, and bornite. At Sugar Loaf, the mineralization is mainly hosted by granite porphyry and syenite protoliths, while at Mutoya is often associated with calc-silicate bodies and argillaceous/ carbonate rocks. Here, sulphides are predominantly pyrite, as dissemination, in veins, blebs or feathers, with chalcopyrite replacing pyrite and bornite. Late pyrite stages are also present, associated with a network of magnetite and quartz-calcite veins.

3. Sampling and analytical methods

3.1. Geophysics

The agreement between BHP Billiton and Blackthorn Resources (AIM Resources) produced in 2004 a Falcon Airborne Gravity Gradiometer (AGG) geophysical survey (Lee, 2001). Almost 9,000 line kilometres of airborne gravity, magnetic, and radiometric data were acquired, flying E-W at 80 m above the ground level, with 400 m line spacing (down to 200 m). The outcome of the survey (Fig. 3) is briefly summarized in the results section.
In addition, we used the regional 250 m grid cell size digital airborne magnetic map of Zambia in order to analyze the magnetic response along the eastern side of the Hook batholith, where the main exploration targets are located. The targets are centred on the N-S striking subrounded to slightly elliptical syenite intrusions that occur at the north-eastern margin of the Hook batholith, and as small intrusions within the pluton (Cikin, 1972; Hanson et al., 1993).
Other syenitic outcrops are shown in regional maps south of the Mwembeshi Zone, within the Zambezi belt (Fig. 1C), and we questioned if more satellite syenite intrusions exist, hidden by the sedimentary cover. In order to investigate such hypothesis, we applied a reduction to pole algorithm to the Total Magnetic Intensity (TMI) regional grid by using the Oasis Montaj software (Geosoft, version 8.0). Filters including analytical signal (AS) and reduced to pole first vertical derivative (RTP1VD) delineate a high-intensity high-frequency aeromagnetic response among the intrusive rocks. Filter processing was combined with line-drawing in order to outline other possible sub-surface syenite satellite bodies.

3.2. Petrography

Seven drillcores from the two mineralized centres have been sampled (Fig. 5A). Although drawing a reliable cross-section is problematic based on the available data, the sampling allowed a better delineation of the outline of the main mineralization and alteration styles. Samples from the five Kitumba drillcores are mainly syenites and quartz-porphyry granites, and most of them show incipient to pervasive alteration, brecciation and hematization. Sample rocks from the two Mutoya drillcores include altered quartz-porphyry syenites, often brecciated, and highly altered metasedimentary rocks.

3.3. Geochemistry

Twenty-two samples from five of the drillcores have been analyzed for major and trace elements. Major elements (and Ga) have been analyzed by X-Ray Fluorescence spectrometry (XRF) at the University of the Witwatersrand, while the other trace elements have been analyzed by ICP-MS at Stellenbosch University. The samples are mainly syenites and quartz-porphyry granitoids, with minor metasediments, and are commonly brecciated. Analytical results are presented in Table 1. For a few highly altered samples where the original lithology is difficult to infer, a question mark appears in the lithology cell.
The rock geochemistry allows for a quantification of the behaviour of major elements with respect to mobility and alteration processes. Specific binary diagrams were used to portray alteration indices, as well as ternary phase diagrams to highlight vectors to alteration and mineralization. Given the degree of alteration of the intrusions of the Mumbwa district, the selection of representative quartz-porphyry granite and syenite protoliths has been based on the data in Milani et al. (2015). Granite sample Z119A, located approximately 25 km west of the town of Mumbwa, was selected as a relatively unaltered precursor for the granite samples. Syenite sample Z48, sampled 60 km to the NW of the town of Mumbwa, is moderately altered but unaffected by massive Fe-oxide replacement, and represents the reference for the syenite-type rocks (sample locations in Fig. 1C).
Sulphur isotope analyses on hypogene and supergene chalcocite, chalcopyrite and pyrite have been performed at the iThemba Labs at the University of the Witwatersrand on 26 samples from the Sugar Loaf and Mutoya mineralized centres. In addition, sulphides form the quartz-monzonite sample Z77 from the Hook batholith have also been analyzed. The sample was collected in a quarry approximately 60 km to the west of the town of Mumbwa (Fig. 1C), and contains pyrite and minor chalcopyrite in secondary veins, and as coatings and selvages (Table 2).

3.4. Analytical techniques

3.4.1. X-Ray Fluorescence (XRF)

Rock samples selected for trace element analyses were washed, crushed (using an iron mortar) and milled to powders. 0.5 g of sample was ignited for 1 hour to obtain LOI and to convert all Fe to the Fe^{3+} state. 0.35 g of the ignited sample was mixed with 2.5 g of Li-metaborate/tetraborate flux and fused for 40 minutes in Au/Pt crucibles at 1000°C and then poured into a mould to produce a perfectly flat analytical surface. XRF method was used for the major elements (Si, Ti, Al, Fe, Mn, Mg, Ca, Na, K, P) and for Ga as a trace element. Analyses have been carried out using the Panalytical Axios (PW2404) WDP XRF spectrometer and samples have been analyzed against calibrations using CRMs (BCR2, BHVO2, BIR1, NIMP, NIMD, NIMS, NIMG, NIML). The matrix correction program is in-house software written by Allan Wilson (University of the Witwatersrand).

3.4.2. Inductively coupled plasma mass spectrometry (ICP-MS)

Fusion disks prepared for routine XRF analysis by an automatic Claisse M4 Gas Fusion instrument and ultrapure Claisse Flux, were coarsely crushed and a chip of sample mounted along with up to 12 other samples in a 2.4cm round resin disk. The mount was mapped, and then polished for analysis.
A Resonetics 193nm Excimer laser connected to an Agilent 7500ce ICP-MS was used in the analysis of the following trace elements: Sc, V, Cr, Co, Ni, Cu, Zn, Rb, Sr, Y, Zr, Nb, Mo, Sn, Cs, Ba, La, Ce, Pr, Nd, Sm, Eu, Gd, Tb, Dy, Ho, Er, Tm, Yb, Lu, Hf, Ta, Pb, Th, U. Ablation was performed in He gas at a flow rate of 0.7L/min, then mixed with argon (0.9L/min) and nitrogen (0.05L/min) just before introduction into the ICP plasma. For traces in fusions, 2 spots of 175 µm were ablated on each sample using a frequency of 10Hz and 100mJ energy.
Trace elements were quantified using NIST 612 for calibration and ^{29}Si as internal standard, using standard – sample bracketing. Two replicate measurements were made on each sample. The calibration standard was run every 10 samples. A quality control standard was run at the beginning of the sequence as well as with the calibration standards throughout. BCR-2 or BHVO 2G, both basaltic glass certified reference standards produced by USGS (Dr Steve Wilson, Denver, CO 80225), was used for this purpose. A fusion control standard from certified basaltic reference material (BCR-2, also from USGS) was also analyzed in the beginning of a sequence to verify the effective ablation of fused material. Data was

processed using Glitter software, distributed by Access Macquarie Ltd., Macquarie University NSW 2109.

3.4.3. Sulphur isotopes

Pyrite, chalcopyrite and a mixture of the two minerals were separated either through drilling or, when disseminated, through crushing, milling, sieving and final handpicking of sulphide flakes. Samples were placed in capsules, and mixed together with vanadium pentoxide (V_2O_5) in a 2:1 ratio to ensure complete combustion. When loaded in the heated tube for gas separation, sample combustion at O pressure and T=1020 °C produces SO_2 gas, which is separated and collected by means of a reduction combustion catalyst. The combustion products move through a helium (He) carrier to a reduction zone to remove oxygen in excess. Then the gas travels through a separate drying tube to remove the excess water. The final products, mainly CO_2, N_2, and SO_2, are separated by gas chromatography, and the SO_2 isotopic ratios are analyzed through mass-spectrometry. The analyses have been performed at the iThemba Labs at the University of the Witwatersrand, using a continuous flow isotope-ratio mass spectrometer (CF-IRMS) connected to a Flash HT plus elemental analyser (EA). The results are presented in δ notation relative to the Cañyon Diablo Troilite. Two standards were used during the investigation to calibrate the mass spectrometer and correct for instrumental drift: CGS–7 (ferrous sulphide) was used to indicate the low delta calibration standard, producing readings of -2.68‰ $\delta^{34}S$; OGS-1 (sulphate) was used as the international standard for high delta calibration, yielding a result of +20.87‰ $\delta^{34}S$. Two standard peak-to-peak models (Brooks et al., 2005) were used to account for the standard deviation for all calibrations, bringing corrections within 0.3‰ $\delta^{34}S$.

4. Results

4.1. Geophysical signature of the Mumbwa district and regional airborne magnetic data of the eastern sector of the Hook batholith

Strong magnetic anomalies (~ 10-100 nT/m, Fig. 3A) characterize both the Sugar Loaf and Mutoya centres and are likely due to the granitoid intrusions. The gravity and magnetic data were also key in outlining the magnetite-hematite zonation characterizing the two centres. Lower-temperature hematite-rich stockworks and breccias appear as gravity highs, whereas peaks in magnetic signature commonly reflect high magnetite/hematite ratios, because of the significantly higher magnetic susceptibility of magnetite (Woolrych et al., 2015). A magnetic signature with peaks at ~ 20 nT/m, coupled with a significant uranium content (57

ppm), characterizes Kitumba (Fig. 3B, Christensen and Whiting, 2013). Conversely, a strong gravity anomaly is lacking at Kitumba (Fig. 3C), which can be accounted for by density reduction processes induced by deep supergene alteration, with weathering reaching up to 700 m depth (Woolrych et al., 2015). The Mutoya s.s. prospect is centred on a high magnetic and gravimetric anomaly (~ 75 nT/m and ~ 10 mGal, respectively, Fig. 3A, C), associated with a moderately high U anomaly (~ 20 ppm, Fig. 3B). To the north, the NNW-SSE-elongated Mushingashi prospect is characterized by an abrupt decrease in magnetic signal, mostly due to the dominant hematization. A persistent gravity high and gravity gradient (~ 14 mGal, Fig. 3C) maps the extent of the iron-rich domain, as well as an extensive zone of manganosiderite alteration to the north. The radiometric signal is negligible (U background at ~ 4 ppm), as a result of the thick sedimentary cover.

At a regional scale, the 250 m grid cell size digital airborne magnetic map of Zambia shows a distinctively high magnetic signal centred on the Hook batholith, due to the abundance of ferromagnetic minerals (mainly magnetite, Naydenov et al., 2014). Manual line-drawing was applied to the magnetic signal to contour domains of different intensity and frequency. Combining these drawings with maps of the analytical signal and reduction to pole-first vertical derivative filtering (Fig. 6A, B), the syenite intrusions appear as very distinctive features, due to their strong magnetic anomalies. The resulting interpretative geological map (Fig. 6C), shows a more extensive array of inferred satellite intrusions, extending ~ 140 km from SE to NW. Also, a ~ 80-km long E-W striking array of slightly E-W elongate magnetic highs can be traced below the Quaternary cover in the Zambezi belt. These are centred on exposed syenites intrusions (Fig. 1C) and show typical magnetic signatures of syenites, and, as such, are interpreted as subsurface syenitic bodies. Only one of the newly mapped syenitic bodies seems to have intruded within the main Hook batholith, whereas the majority of the bodies are located about 10-12 km east and SE of the batholith.

The inferred larger distribution of the syenitic bodies, which are commonly associated with mineralization, might open new perspects for exploration, in particular to the south of the Mwembeshi Zone, where investigations for commodities have been limited in recent years.

4.2. Petrography

Syenite rocks from the Kitumba prospect are predominantly feldspar-porphyry, ranging in colour from red-orange to grey-pinkish, according to the extent of alteration. In relatively unaltered types, the main phases are tabular orthoclase, quartz and anhedral plagioclase, with biotite and amphibole as main mafic minerals, and Fe-Ti-oxides, apatite and zircon as accessories. Secondary calcite and epidote often occur both interstitial or in veinlets. Severe alteration produced extensive sericite replacement of plagioclase and microcline, iron

staining on feldspar and hornblende growing on biotite. Iron-oxide overprinting in some cases completely obliterated the original syenitic fabric. Quartz-porphyry granite is characterized by quartz phenocryst, microcline and minor plagioclase in a quartz-feldspar-rich groundmass. Biotite and amphibole are common, and late iron oxides are interstitial, or replace feldspar phenocrysts. Alteration is mainly expressed as sericitization of feldspar Siliciclastic quartz-sedimentary breccia in a hematite matrix, which is also part of the Kitumba samples, was also largely affected by carbonate, silicification and sericite alteration. Among Mutoya samples, porphyritic syenite commonly shows pervasive phenocryst sericitization, with massive magnetite replacement zones and sericite-chlorite patches largely obliterating the original texture. Metasedimentary samples are mostly clast-supported polymictic breccia cemented by magnetite, and these show texturally destructive calcite, epidote and chlorite alteration. In places, a silicification overprint is pervasive, and late Fe-oxide and calcite veins are also common.

4.3. Tectonic features, mineralization, brecciation and alteration in the Mumbwa district

Copper mineralization preferentially developed at fault intersections, in close association with the syenitic satellite intrusions. Most of the syenitic rocks appear extensively altered, with a typical salmon-pink colour due to K-feldspar groundmass replacement [K_2O > 10 wt%, compared to 6-7 wt% for unaltered syenites, e.g. Lobo-Guerrero Sanz (2005) and Milani et al. (2015)].

The hypogene sulphide assemblage was overprinted by a pervasive supergene mineralization, whereas, at the surface, weathering and leaching formed a thick saprolitic cover accompanied by development of clay minerals and Fe-Mn-Cu hydroxides in vuggy and/or brecciated textures (Robertson, 2013; Waller et al., 2014). Large amounts of iron were involved in the hydrothermal processes, leading to a large-scale zonation defined by magnetite- and hematite-rich domains.

Hydrothermal breccias are another distinctive feature of the Mumbwa district (Fig. 7A-D). Breccias involve metasedimentary as well as intrusive rocks, and often host the mineralization. They can be matrix- or clast-supported, and are in many places within, or peripheral to, fault zones (Robertson, 2013; Waller et al., 2014). Breccias range from incipient crackle, jigsaw, and mosaic textures with no displacement of angular to sub-angular fragments (crackle brecciation, Fig. 7B), through clast-supported polyphase breccias, to chaotic breccias where larger clasts are set in a groundmass of smaller fragments (Fig. 7C). In general, the abundance of angular clasts derived from a proximal host rock does not provide evidence of transport, and suggests that the brecciation mechanism was either induced by volatile exsolution and/or expansion of over-pressured fluids.

An estimation of the extent of the alteration zones in the Mumbwa district is not possible, as most of the observations on alteration styles are localized to the drilled areas. Selectively pervasive to pervasive potassic alteration affects the district and is documented in more distal areas (Milani et al., 2015). Sericite (± chlorite) alteration and superimposed carbonate (± magnetite-amphibole-apatite) are also observed, and sodic phase alteration to albite or scapolite has been occasionally described in the Hook area (M.W. Hitzman, pers. comm., 2008; R.H. Sillitoe, pers. comm., 2010).

4.4. Kitumba prospect (Sugar Loaf centre)

The Sugar Loaf centre is characterized by extensive hydrothermal iron oxides, with pervasive magnetite alteration to the south (i.e. Sugar Loaf mine), and deep-level magnetite plus shallow-level hematite alteration to the north, at the Kitumba prospect (Robertson, 2013; Waller et al., 2014).
Most of the recent mining activity has focused on the Kitumba mining license that covers an area of approximately 250 sq. km. The deposit is located 2.5 km NW of the old Sugar Loaf mine, centred on the Hook porphyritic granitoids and syenites intruded into Kundelungu Group metasiltstones and metaargillites (Fig. 5B).

4.4.1. Structural setting

The Kitumba Fault Zone represents the main structural feature, displaced from the Mumbwa Fault Zone by the ENE-striking Kankamu Fault (Fig. 2, 4, 5B). Recent studies on drillcores indicate that the fault system is sub-vertical to steeply W-dipping at the surface, flattens at ~ 500 m depth and involves a component of thrusting (Fig. 5C). Oblique-reverse SSE-dipping faults cut the Kitumba Fault system (Fig. 5B), and were likely to have been re-activated after ore deposition, as breccias and alteration facies appear displaced with a S-side-up dip-slip component (20-200 m) and a dextral strike-slip component (80-200 m; N. Hayward, pers. comm., 2008). At the intersection between the Kitumba Fault Zone and the ENE-striking faults, hematite breccias associated with copper mineralization are common. This suggests a pre- to syn-mineralization timing of faulting, and indicates that the intersection zones are critical vectors to mineralization (N. Hayward, pers. comm., 2008).

4.4.2. Hypogene alteration

An alteration system centred on stockwork veins has been proposed, with distinct hypogene alteration facies zoned approximately from deeper-hotter-older (magnetite-dominated, prevalent to the south of Kitumba and towards the Sugar Loaf mine) to shallower-cooler-

younger facies (hematite-dominated, to the north) in the order: magnetite, K-feldspar, carbonate, hematite, sericite ± chlorite (Fig. 8; Robertson, 2013 and references therein). The paragenetic sequence of the main alteration phases at Kitumba, both hypogene and supergene, is summarized in Table 3.

- Magnetite alteration

Coarse grained magnetite (± apatite, amphibole, biotite) replacement characterizes breccias and stockwork veins, producing a strong magnetic anomaly at the southern end of the Sugar Loaf centre (Fig. 3A). Amphibole (5-60% vol.) includes coarse prismatic pale-green crystals (probably tremolite-ferroactinolite series), whereas biotite (0-30% vol.) is fine to medium-grained. Apatite (up to 25% vol.) can form centimetre-size euhedral crystals. Other accessory minerals include aegirine-augite, calcite, albite, specular hematite, pyrite, chalcopyrite and rare cordierite.

- Potassic alteration

Potassic alteration is widespread, ranging from selective feldspar replacement to pervasive and texturally-destructive alteration. Its areal extent is unknown, but it mostly affects the feldspar-rich porphyry syenite bodies, resulting in a salmon pink to reddish feldspathic groundmass which hosts euhedral to subhedral feldspar phenocrysts, subsequently partially sericitized/carbonatized (Fig. 9A). Similar potassic alteration is observed in the metasediments to the north-west of the Mumbwa area and within the hematite breccias. Accessory minerals include carbonate, biotite, specularite and chlorite. The alteration zone appears to be bound to the east by the Kitumba Fault Zone, where displacement along the fault system placed potassic altered and non-potassic altered fault blocks adjacent to each other. This suggests that potassic alteration occurred early in the life of the Kitumba Fault system and was not active in the later phases of reactivation when hematite alteration was prevalent. The potassic alteration zone is open to the west of Kitumba, but has been noted to decrease in intensity.

- Carbonate alteration

Carbonate alteration is common and two main varieties have been identified. A strong carbonate (ankerite) alteration occurs in the syenite and porphyritic granites, mainly as pervasive texturally-destructive, coarse-grained replacement carbonate. Polymict breccias and brecciated syenites may have been almost totally replaced by carbonate. Such alteration is abundant throughout the hypogene zone and often occurs in association with potassic and sericite alteration, but it is absent in highly altered hematite zones and in kaolinite-rich zones. The second type consists of late carbonate (siderite-ankerite) veining crosscutting hematite, K-feldspar and sericite alteration. The veins are usually siderite-rich within the Kitumba deposit proximal to the Kitumba Fault Zone, becoming more calcium-rich,

with calcite and ankerite, distal to the deposit. Both siderite and ankerite veins are often in association with pyrite and chalcopyrite. Locally, carbonate replacement appears as orbicular grains, 1-2 cm in diameter, partially silicified, with fine specular hematite in the interstices. At times, carbonate replacing coarse prismatic crystal aggregates (actinolite?) have been observed (N. Hayward, pers. comm., 2008).

- Hematite alteration

Hypogene hematite alteration is widespread, in particular proximal to the Kitumba Fault Zone, where fine- to medium-grained specular hematite (± pyrite, chalcopyrite, sericite, carbonate, quartz) can pervasively replace both clasts and matrix in the breccias. When peripheral to the core breccia zones, primary hematite occurs as veins and blebs. Pyrite as disseminations, in veins, or even as masses is the most common accessory mineral in hematite altered zones. In places, it can form 50% of the breccia volume. Textural evidence shows that hematite alteration is superimposed on the other alteration types and extends across a wide vertical range along the Kitumba Fault system (Waller et al., 2014).

- Sericite alteration

Sericite (± chlorite) overprints potassic alteration, and has been documented also at depth. It is more prevalent in the distal portions of the prospect, in particular towards the est, but it is not documented immediately to the east of the Kitumba Fault Zone. Fine-grained, cream coloured sericite appears in semi-pervasive matrix replacement, or as selective replacement of feldspar phenocrysts. Sericite (± chlorite) alteration can be so pervasive as to obliterate all the original phases. Relicts of biotite and amphibole are only rarely visible, and only the large quartz grains are usually well preserved. At the contact with the metasediments, the syenite bodies show a complex mixture of texturally destructive alteration including sericite, chlorite, carbonate and hematite, frequently associated with sulphide mineralization (Fig. 9B). Accessory phases are fine-grained hematite, carbonate, quartz, chlorite, pyrite and chalcopyrite.

Besides the main alteration zones, silicification has been observed in crackle breccias, or as late quartz veins cutting primary phenocrysts or iron oxides. Locally, thick (tens of m) gently-dipping tabular bodies of apatite-Fe-carbonate-hematite intergrowths have also been documented. These bodies, presumably of hydrothermal origin, often fringe the ore zone and might be considered a valid marker for exploration (Fig. 9C).

4.4.3. Supergene alteration

The supergene activity at Kitumba was certainly exceptional, as weathering effects have been observed down to 700 m depth. Weathering has been preferentially focused vertically down the Kitumba Fault Zone and where occurring along horizontal fractures, ‘core stones’

of relatively fresh rock have been left. In the thick saprolite cap at the surface, which is up to 100 m, there has been extensive textural destruction and clay alteration. Secondary iron alteration, induced by weathering and percolating iron-rich meteoric fluids, produced brick-red mottled hematite aureoles and yellowish mottled goethite stains affecting hematite and pyrite veins. Secondary hematite is also common as martite after hypogene magnetite or as steely hematite occurring at shallow levels. Stains or veins of Cu-rich Mn-oxides are also distinctive supergene phases at Kitumba. Weathering processes also resulted in kaolinite replacement of K-feldspar and sericite, goethite replacement of Fe(Cu) sulphides, vugs after leaching of carbonate and sulphides, and a large number of supergene Cu-rich minerals (see 4.4.5.).

4.4.4. Hypogene mineralization

The 200-450 m-wide copper-rich zone at Kitumba extends over an approximately 2 km-long, N-S-striking corridor. The entire Cu shell forms a steeply E-dipping system (Fig. 5C and Waller et al., 2014), whereas the ore distribution conforms locally to the syenite orientation, roughly following shallow W-dipping planar surfaces (Fig. 5C). The hypogene ore is relatively low grade, averaging between 0.4-0.8% Cu. Two styles of mineralization are predominant:
i) Breccia-hosted sulphides: pyrite and subordinate chalcopyrite are disseminated in hematite breccias which overprinted and dismembered a potassically altered syenitic or quartz-porphyry granitic protolith. In places, hematite-breccia clasts have been replaced by pyrite (Fig. 9D). Sulphides developed mostly post-brecciation and post-hematite and partially replace clasts, or are disseminated in the groundmass associated with hematite.
ii) Sulphides in veins: pyrite and chalcopyrite appear as stockwork veinlets (Fig. 9E) and frequently occur in association with carbonate, hematite, siderite and quartz.

4.4.5. Supergene mineralization

Pervasive supergene copper has been observed in boreholes where it is mainly associated with a variably hematite-brecciated syenite rock. The enhanced permeability at the intersection between the Kitumba Fault Zone and ENE-striking faults is supposed to have favoured copper remobilization and concentration (Waller et al., 2014). The most common supergene copper minerals are native copper in veins and vugs (Fig. 9F), and malachite in fractures and disseminations (Fig. 9G). These are accompanied by chalcocite, copper phosphates, cuprite, covellite, digenite, chrysocolla, bornite, limonite and Cu-rich Mn-oxides. The zones of strongest supergene enrichment are usually characterized by chalcocite in veins in association with pyrite or native copper, in stockworks with bornite, or in the cores of

malachite and pseudomalachite, together with minor bornite and malachite after chalcopyrite. Chalcopyrite commonly rims pyrite, or partially replaces it, or is interstitial to, pyrite grains (Fig. 9H). It also form blebs and disseminated patches within the host rock. Locally, massive chalcopyrite has been observed in brecciated lithologies whose primary phases were pervasively replaced by oxides, with extensive sericite (± chlorite, epidote).

4.5. Mutoya centre

Mutoya s.s. consists of a calc-silicate body of two sq. km with sporadic porphyritic intrusions and brecciated feldspar-rich porphyritic dykes interpreted as apophyses of larger syenitic bodies that have been intersected at depth (Fig. 5A). The skarn-type mineralogy includes epidote, actinolite and biotite, and accessory diopside, garnet, apatite, wollastonite, and is inferred to have been produced by interaction between the intrusions and the Katanga Supergroup metasediments (R.H. Sillitoe, pers. comm., 2010). Metasediments appear as arenitic to argillitic siliciclastic sequences and, where finely laminated, they are potassically altered, with patchy K-feldspar in addition to epidote, chlorite, sericite, and biotite. Large areas of intense magnetite-amphibole-apatite-carbonate alteration are widespread (Fig. 10A). A later stage of hydrolytic alteration affected both metasedimentary and intrusive rocks, as indicated by the formation of sericite after K-feldspar and chlorite after calc-silicate minerals. Skarns, hornfels and porphyritic rocks are cut by late magnetite veins (up to few metres-wide, Fig. 10B). Large breccia zones may extend for several kilometres, and sporadically contain minor pyrite (up to 15% vol.). Breccias are mainly polymict, dominated by unsorted metasedimentary clasts, and cemented by calcite, magnetite and minor pyrite. Breccias involving a mixture of an igneous protolith and carbonate/pelitic clasts have also been observed. Magnetite was replaced by steel-grey specular hematite, which is common as centimetric veins and stockworks. This stage was followed by the main sulphide event with predominant pyrite, and minor chalcopyrite, observed as cm-wide stockworks and blebs, or as replacements of pyrite. Occasional bornite has been documented in quartz-carbonate-chlorite-magnetite veinlets, whereas no obvious supergene overprint has been observed.

North of Mutoya s.s., the Mushingashi prospect is characterized by intermediate to felsic porphyritic intrusions, and, further north, by a massive hematite-siderite system, mainly hidden by 250-350 m of Karoo sediments. The main porphyritic body has been estimated as 5 km-long and up to 900 m wide. Its original composition is difficult to assess, but based on the abundance of plagioclase and pyroxene relicts, a diorite protolith has been inferred (R.H. Sillitoe, pers. comm., 2010). The rock is microcrystalline and is affected by pervasive calcic and potassic alteration, with diopside and minor garnet overprinted by actinolite, epidote, K-

feldspar and biotite, and late chlorite alteration commonly replacing mafic minerals and feldspar. Rock colour varies from brick-red to greenish, according to the predominance of K-feldspar or chlorite-epidote alteration. More felsic rocks are characterized by up to 25 wt%, euhedral feldspar phenocrysts, 10 wt% quartz and by pervasive sericite replacement, including of the groundmass. A steep 5 km-long, N-S-striking, and up to 250 m wide, tabular massive body of magnetite is developed around the main intrusive body. Millimetre to cm-wide magnetite stockwork veins are frequent and commonly host late-stage quartz, calcite and pyrite mineralized lenses (Fig. 10C). Matrix to clast-supported hydrothermal breccias have been observed in various drillcores. Magnetite-cemented breccias with igneous clasts altered to chlorite, carbonate and epidote are common. They are partially silicified and, occasionally, host disseminated and blebby pyrite and chalcopyrite.

Average copper content at the Mutoya centre is 0.1%, increasing up to 0.2% in isolated supergene chalcocite enrichment zones. Sulphides, mainly as pyrite with Py/Ccp ~ 10, occur as large euhedral crystals associated with quartz or calcite veins, or, where in massive magnetite, as disseminated selvages to feathery to spherulitic textures (Fig. 10D). Abundant specularite as needles and elongated grains is common (Fig. 10E), whereas late chalcopyrite developed either interstitially in anhedral patches, or rimming large pyrite crystals (Fig. 10F). Bornite on botryoidal chalcopyrite replacements has also been observed (Fig. 10G).

The northern extension of the Mushingashi prospect progressively grades into a hematite-dominated zone, that has developed into a N-S, 10 km-long, elongated body of massive, fine- to medium-grained, light brown-coloured manganosiderite. Remnants of dolomite-argillaceous rocks, considered as the rock precursor, have been observed. Medium-grained chloritized dioritic dikes were intersected throughout the anomaly. Hematite, often as specularite, is the dominant oxide replacement mineral, commonly superimposed on already altered metasediments. Hypogene sulphides, mainly as disseminations, are dominated by pyrite and minor chalcopyrite, mostly confined to the manganosideritic body and to the diorite dykes. A 200 m deep supergene zone has been preserved in the northernmost sector, characterized by red-brown to black earthy hematite, and by conversion of pyrite and chalcopyrite into limonite. Minor amounts of chalcocite, bornite, copper oxides and carbonates are concentrated in late fractures.

4.6. Major and trace elements

The geochemistry, location and depth, lithology, and main alteration types of the analyzed samples are summarized in Table 1.

The SiO_2 content varies from 25 to 82 wt%, and we infer that the range does not reflect the original silica but the variable extent of Si and Fe loss or gain, as well as the amount of loss on ignition (LOI). TiO_2 spans one order of magnitude, from 0.14 to1.32 wt%. Iron is usually high, with metasedimentary rocks and breccias retaining the highest contents, reaching 47.3 wt% FeO in sample MUM4D/6. Massive iron replacement zones were avoided during sampling. Nevertheless, the iron content can be influenced by the presence of magnetite or hematite patches (as in sample MUM4D/6), and caution must be adopted in interpreting the results. MnO is often above 1 wt% when measured in highly oxidized rocks, while MgO is erratic, with values constrained between 0.11 and 7.6 wt%, according to the different degree of chloritization. CaO is enriched in samples affected by carbonate alteration or in calc-silicates, but appears depleted in many of the analyzed samples. Na_2O has been almost totally removed. Its content never exceeds 0.48 wt% and, occasionally, is below the detection limit. The pervasive potassic or sericitic alteration results in K_2O being generally higher in the analyzed samples (>10 wt%) than in the inferred protoliths (Table 1), and P_2O_5 shows values that reach up to 0.71 wt% in the most altered samples, in particular in association with apatite, chlorite, epidote and actinolite.

The effects of superimposed alteration processes have been assessed by applying the isocon approach of Grant (1986) and by comparing the inferred granitic and syenitic protoliths with the samples preserving sufficient chemical and texture features indicative of a syenitic or granitic nature. The method allows for an evaluation of the degree of element mass loss or gain by eliminating the effect of a simultaneous increase or decrease in volume occurring during alteration. Although the inferred protoliths cannot be considered completely unaltered, the method applied to the major elements provides useful insights into the geochemical changes induced by alteration. The results are shown in Fig. 11 and Table 4. Granite-derived samples show a moderate to relevant volume increase, as revealed by isocon slopes < 1 (Table 4). Silica enrichment is apparent in all the quartz-porphyry granites, with a wt% mass gain from 33 to 99% (Fig. 11A and Table 4), and is documented by the common growth of authigenic euhedral quartz. The TiO_2 content is either stable, or drops remarkably, whereas Al_2O_3 is substantially unchanged. The Fe-oxidation effect is relevant only in hematite-rich sample S36_33/7A. Where MnO content increases, it is not paired with an FeO increase, indicating development of Mn-oxides. K_2O gain is driven by potassic and sericitic alteration, whereas the increase in P_2O_5 is related to apatite growth. MgO, CaO and especially Na_2O are ubiquitously depleted.

Syenite-derived rocks (Fig. 11B) appear substantially unchanged in volume, except for a decrease in sample MUM4D/7 (Table 4). As with the granitic samples, syenites show depletion in MgO, CaO and Na_2O, enrichment in K_2O, and P_2O_5 from unchanged to enriched. SiO_2 mass slightly decreases, while TiO_2 tends to increase, or is unchanged.

Syenites also show a relevant FeO increase, due to hematization, and a MnO spike indicating Mn-oxide growth.
As to the trace elements, the enrichment in Ba and Rb in altered igneous samples compared to the inferred protoliths is interpreted to have resulted from potassic alteration. A peak in Sr is found in epidote-rich samples, and high contents are also shown for Cu-Zn (related to sulphides), Co-Mo-Ni (pyrite), Zn-V (titanomagnetite). Uranium and Th enrichments, with decreasing or stable Pb, are responsible for the high U/Pb and Th/Pb ratios. An enrichment in LREE is observed in most of the Kitumba samples, whereas REE mobility is not particularly significant at Mutoya, as altered magmatic rocks commonly retain patterns which are smooth and comparable to the REE distribution of the inferred protoliths (Fig. 12). More data are needed in order to verify if a different behaviour as to LREE distribution exists between the two areas. The low REE content of Mutoya s.s. sample MUM4D/6 is related to the high magnetite content - notably a low-REE mineral - of the analyzed rock powder.

4.7. Sulphur Isotopes

A summary of isotope values, together with details on geographic location, mineralization type, host rock, sulphide assemblage, and alteration is presented in Table 2. All $\delta^{34}S$ values lie between +1.4 and +7.6‰ relative to the Cañon Diablo Troilite (CDT), while the unaltered Hook quartz-monzonite shows a slightly higher value, at +8.6‰. No difference is recorded among the analyzed sulphides (Py, Ccp, Cc), between hypogene and supergene mineralization, or with depth. However, it is notable that at Kitumba, $\delta^{34}S$ is constrained between +4.3 and +7.6‰, whereas at Mutoya s.s. and Mushingashi the values are generally lower, in the range +1.4 and +4.4‰.

5. Discussion

5.1. IOCG affiliation

The growing interest of the industry and scientific community in IOCG-type deposits is justified by the resource potential that many of them offer, often exceeding 500 Mt (million metric tons) at higher copper grades than those of most porphyries of comparable tonnage (Groves et al., 2010). Many of the richest iron oxide copper gold (IOCG) deposits are hosted in Precambrian terranes (e.g., Gawler craton and Cloncurry district, Australia; Carajás, Brazil). They are generally associated with anorogenic or intracratonic environments (e.g., Groves et al., 2010), but back-arc or foreland settings have also been suggested (Haywood, 2008; Skirrow, 2008). A convergent margin environment is invoked for some significant

Phanerozoic deposits, such as Candelaria-Punta del Cobre and Mantoverde, Chile (Barton, 2014). It is also suggested that IOCG-type deposits can develop together with iron-apatite-rich deposits (Kiruna-types, IOA) as a part of a single ore-forming system, with IOA representing the deep roots of an IOCG system (Hitzman, 2000; Edfelt and Martinsson, 2003; Sillitoe, 2003; Williams et al., 2005; Day et al., 2016; Barra et al., 2017; Simon et al., 2018).

Despite such interest, the high variability in tectonic settings, chemistry and depositional styles still prevents full clarification of key parameters, like the mechanisms relating regional hydrothermal systems to localized copper-gold deposition, the role played by intrusions, host rocks and basinal or meteoric fluids, the debated sources of sulphur and metals, and the occurrence in tectonic settings which vary from intra-cratonic to continental margins (Williams et al., 2005).

An IOCG geological model has been proposed for the deposits of the Mumbwa district (Robertson, 2013, and references therein) but no critical review of the characteristics of Sugar Loaf and Mutoya centres that could account for its classification as an IOCG has been presented so far.

In terms of iron enrichment, the differentiation between magnetite- and hematite-rich zones with depth is considered a common feature of IOCG deposits when both Fe-oxides are present (Barton and Johnson, 2004; Barton, 2014), and, except for the lack of a deep Na alteration at Kitumba, the vertical zonation of alteration styles roughly corresponds to the metasomatic footprints commonly highlighted in IOA-IOCG deposits (Montreuil et al., 2013).

The affiliation of the Mumbwa district to the IOCG group can be considered following the criteria of Groves et al. (2010), which highlights comparisons and contrasts. The following requisites are verified:

i) Structurally-controlled hydrothermal system, in association with breccias: in the studied area, the magnetite or hematite-dominated hydrothermal breccia system developed along the Mumbwa Fault Zone. At Kitumba, the steeply W-dipping to subvertical Kitumba Fault Zone is cut by an array of subparallel SSE-dipping faults (Figs. 2, 4, 5B). These structures preferentially concentrated Cu (± Au) along their strike and/or at their intersections.

ii) Cu content between 0.7 and 1.5% in hypogene ore [in world-class deposits, see also Williams et al. (2005); Grainger et al. (2008)]: at Kitumba this is verified in numerous drill cores (Robertson, 2013). A 3D estimation of the extent of the hypogene Cu > 1% shell was calculated from the interpolation of core logs (Waller et al., 2014 and Fig. 5C). From the updated JORC Code (2012) a compliant Mineral Resource estimate at 1% copper cut-off grade, the Measured and Indicated hypogene Cu content is estimated at Kitumba at 2.06% (Intrepid Mines Ltd report, 2015).

iii) Close spatial association of sulphide mineralization with calcic and potassic alteration: potassic alteration is widespread and in the Hook area it extends at a regional-scale well outside the mineralized system, as documented in Milani et al. (2015).
iv) Lack of widespread syn-sulphide quartz veins or silicification: large-scale silicification zones are not found in the Mumbwa district although quartz is a common component of breccias. Lenses, wisps, stockworks and discontinuous micro-veins of quartz are commonly associated with sulphides ± siderite and/or hematite, and irregular patches or veinlets of quartz are commonly associated with the quartz-feldspar syenite. However, these occurrences are very minor compared to the size of the hydrothermal system.
v) Abundance of low-Ti iron oxides (magnetite, hematite) and iron silicates associated with Fe-Cu sulphides: Fe-oxides characterize the mineralogy of the district. As to iron silicates, actinolite is common in the alteration paragenises (no data on the mineral composition are available).
vi) High light rare earth element (LREE) content: although based on a limited number of data, this is verified in the samples of the Kitumba prospect (Fig. 12).
vii) Temporal (although not necessarily spatial) relationships to magmatic intrusions: in the Mumbwa district, a spatial association between copper mineralization and syenite-dominated bodies is apparent. A temporal relationship is less constrained, but at Kitumba a case where sulphide-bearing stockwork veinlets in syenite terminate against a younger syenite pulse suggests a sequential relationship where the sulphide-rich veins are bracketed within two temporally different syenitic events.

In contrast, the following features that typify IOCG deposits (Groves et al., 2010) are not verified at Mumbwa:
i) Hypogene gold content in the range 0.1 - 0.6 g/t (in world-class to giant deposits): the highest Au contents were recorded at Kitumba, with a total of 68 m at 0.10 g/t Au after the 1990's Billiton campaign (Christensen and Whiting, 2013); 18 m at 0.20 g/t Au intersected in log S36_1 (phase 2, Woolrych et al., 2015); 14 holes above the 0.25 g/t Au cut-off grades (phase 3, Woolrych et al., 2015); 11 m with Au > 0.5 g/t in two drill cores (S36_39, S36_40, phase 5, Blackthorn Resources report, 2014). According to the JORC Code (2012) estimate, the total (hypogene + supergene) Au content does not exceed 0.04 g/t (Intrepid Mines report, 2015).
ii) Low pyrite (or high-S sulphides) content: Mutoya s.s., Mushingashi and part of Kitumba show high pyrite/chalcopyrite ratios.
iii) Association with early extensive sodic or sodic-calcic alteration which may form large, irregular zones: although albite or scapolite have been occasionally described in the Hook area (M.W. Hitzman, pers. comm., 2008; R.H. Sillitoe, pers. comm., 2010), none of the

prospects in the Mumbwa area shows pervasive Na- or Na-Ca- alteration. Where Ca is introduced, it is not paired with Na, and is either related to carbonate siderite-ankerite as at Kitumba, or to the development of calc-silicate minerals, in particular epidote, as observed at the Mutoya centre.

The paucity of economic Au contents and the high pyrite/chalcopyrite ratio appear to be the most significant detractors from an IOCG affiliation of the investigated prospects, while the local abundance of bodies and veins of apatite + Fe-oxides (+ Fe-carbonates) are more akin to the Kiruna-type iron oxide-apatite (IOA) deposits. No specific features unequivocally distinguish between economic IOCG occurrences and large-scale magnetite/hematite bodies with low Cu-Au contents (Kiruna-type), and it is unclear whether the latter type is related to geochemically unfertile conditions, or to inefficient structural/geochemical traps. Although a genetic link between IOCGs and IOAs remains controversial (Knipping et al., 2015), many authors consider IOAs as the Cu-poor end member of the IOCG-type deposits (Hitzman et al., 1992; Barton and Johnson, 1996; Williams et al., 2005; Mao et al., 2016; Simon et al., 2018).
Nevertheless, in this contribution, we concur with the historical classification of the Mumbwa deposits and although the Sugar Loaf and Mutoya centres lack significant gold or sodic alteration, we now regard these mineralized centres as IOCG-types and we review the controlling parameters and triggering mechanisms of the Mumbwa mineralization in the light of the current knowledge of IOCG systems. With respect to the pyrite-rich, magnetite (-amphibole-apatite-carbonate) alteration zones at depth at Kitumba and north of the Kankamu Fault, it is also possible that they represent the remnants of a Kiruna-type (IOA) stage of alteration on top of which an IOCG system evolved (e.g., Montreuil et al., 2013; Corriveau et al., 2016).

5.2. Sulphur and metal sources

Low pH, highly oxidized, saline, sulphide-poor fluids with up to 50 wt% eq. NaCl (Groves and Vielreicher, 2001 and references therein) are required to generate an IOCG system (Barton and Johnson, 2004). In these systems, fluid salinity and temperature are the main controllers of Fe solubility (e.g., Chou and Eugster, 1977; Hemley et al., 1992; McPhail, 1993; Sverjensky et al., 1991), but also host-rock interaction, changes in pressure, pH and Eh play an important role (Mark et al., 2006).
In terms of fluid sources, two main families can be distinguished: magmatic and non-magmatic sources (Barton and Johnson, 2004). The main role played by sulphur in precipitating sulphides and its particular isotopic chemistry can help in inferring the nature of

the fluid source(s). It is accepted that $\delta^{34}S$ values around 0‰ indicate a magmatic (igneous) origin for sulphur (Seal, 2006; Barton, 2014). These conditions are commonly preserved in a reduced environment, where sulphur is mobilized as sulphide (H_2S, HS^-). However, given the common oxidized nature of the IOCG systems, it is only in a few specific cases that dominant reduced conditions proved to be the controlling factor, in particular in the presence of hydrothermal pyrrhotite, and in uncommon very high-T magnetite-rich assemblages (Chen, 2010). The presence of hematite indicates a higher oxidation state, and suggests a sulphate-dominated system where sulphur was transported as SO_4^{2-}, HSO_4^- or $NaSO_4^-$. This is the case with sulphate-bearing evaporitic brines, which carry abundant sulphate complexes (Ohmoto and Rye, 1979), and whose $\delta^{34}S$ is commonly assumed to have been 5-15‰ higher than of any coexisting sulphides (e.g., Bastrakov et al., 2007).

The sulphur isotopic data at Mumbwa, constrained between +1.4 and +7.6‰ (Table 2), suggest interaction between magmas ($\delta^{34}S$ ~ 0‰) and saline brines trapped in the Katangan sedimentary sequence, resulting in an increase in $\delta^{34}S$ values. No direct evidence of evaporites is reported in the Mumbwa area, but evaporitic sabkha facies, anhydrite and gypsum relicts, together with collapse breccias, are common at the base of the Katanga Supergroup (Upper Roan Subgroup, Annels, 1974; Selley et al., 2005; Bull et al., 2011).

No apparent isotopic difference exists between hypogene and supergene sulphides, or within different sulphides. However, sulphides at the Kitumba prospect retain $\delta^{34}S$ values commonly higher than at the Mutoya centre. Interestingly, at Kitumba sulphides are hematite-dominated, whereas at Mutoya s.s. and Mushingashi sulphides are associated with massive magnetite, which is an indicator of higher temperature and greater depth conditions (Barton, 2014). The isotopic differences among the prospects can be tentatively explained by a stronger influence at Kitumba of an evaporitic brine interacting with a magmatic fluid. The exotic, non-magmatic fluid would have preferably penetrated to a shallower depth and towards the peripheral, typically hematite-rich parts of the ore system. A similar isotopic differentiation has been observed in the IOCG deposits of the Mantoverde district, Chile (Rieger et al., 2010), at Raúl-Condestable, Peru (De Haller and Fontboté, 2009), and also in the Candelaria-Punta del Cobre district, Chile, where predominant sulphides with an igneous signature (Marschik and Fontboté, 1996, 2001; Mathur et al., 2002) are locally accompanied by comparatively higher $\delta^{34}S$ ratios at shallow depths (~ 7.0‰, Ullrich and Clark, 1999).

A role of purely evaporitic components at Mumbwa seems unlikely, as non-magmatic IOCG systems show a wider range of sulphur isotopic values than were found at Mumbwa (Hunt et al., 2007). In addition, these brines can carry significant iron and metals, but require additional sulphur to trigger deposition of copper and other chalcophile elements (e.g., Barton, 2014). Also, the hypothesis of an igneous contribution is consistent with magmatic fluids being commonly associated with K-rich alkaline protoliths, collisional settings and

limited Na alteration (Barton and Johnson, 2000). Indeed, magmatic fluids associated with ore formation have been inferred, for example, in the Cloncurry district (Rotherham et al., 1998; Mark et al., 2000; Baker et al., 2001; Williams and Pollard, 2003; Duncan et al., 2011, 2014), and at the Olympic Dam deposit (Johnson and McCulloch, 1995; Skirrow et al., 2002, 2007).

The available data do not allow any discrimination between the possible metal source(s), so hypotheses are highly speculative. One possibility is that the metal-bearing fluids were low T (75-220 °C), hematite-stable (oxidized), chloride-rich, sedimentary brines, that could have carried large quantities of iron and metals in a sulphur-deficient fluid (e.g., Barton, 2014). These brines could have leached copper and other metals from continental red beds, as inferred for the lower part of Katangan sequence in the Zambian Copperbelt (Selley et al., 2005; Zientek et al., 2014) and from mafic rocks, with sulphide precipitation at a redox boundary induced by organic material or sour gases such as hydrogen sulphide (Hoy and Ohmoto, 1989; Hayes et al., 2012). This hypothesis is consistent with the occurrence of mafic intrusive rocks within the Hook batholith (Fig. 1C), and with the inferred Hook granite emplacement at shallow crustal levels (Milani et al., 2015 and references therein).

A second possibility is that the metals were derived from the felsic magmas, as magmatic fluids are considered a major contributor to ore formation in many IOCG deposits (Whitney et al., 1985; Pollard, 2006; Groves et al., 2010). The abundance of primary magnetite in the granitoids of the Hook batholith (Naydenov et al., 2014), coupled with the sulphur isotopic signatures, support this hypothesis. Metal precipitation would then have been a function of oxidation state and fractionation degree of the melt (Lehmann, 1990; Blevin and Chappell, 1992). In a reduced environment, as in ilmenite-bearing granites, early removal from the melt of Cu and Au, Mo, Co, Ni tends to prevent significant Cu-Au mineralization (Pollard, 2006), whereas more oxidizing conditions favour copper-rich fluid saturation and consequent mineral deposition (Candela, 1989).

5.3. Alteration and mineralization vectors

As a broad generalization, the alteration of IOCG systems follows a vertical zonation, with sodic (± calcic) alteration commonly prevailing at deeper (and peripheral) levels, potassic and potassic-calcic at intermediate to shallow levels, and sericitic alteration (± silicification) at very shallow levels (Barton, 2014). Magnetite will be predominant at depth and at higher T, with chalcopyrite, pyrite, and pyrrhotite as the main sulphides (Pollard, 2006; Barton, 2014). At shallower levels, the mineral assemblages indicate more oxidized and lower temperature conditions, and hematite with chalcocite + bornite can become significant (Hitzman et al., 1992). This transition is often interpreted as time-dependent, as suggested in

the Olympic Dam district (Oreskes and Einaudi, 1992; Bastrakov et al., 2007) and confirmed through field observations and thermodynamic modelling (Gow et al., 1994; Bastrakov et al., 2007; Belperio et al., 2007; Ehrig et al., 2013).

Precipitation of magnetite (± apatite, actinolite) requires temperatures above 500°C (Barton, 2014) but, in a few exceptions, temperatures exceeding 800°C have been inferred, based on isotopic and fluid inclusion thermometry (e.g., Broman et al., 1999; Velasco and Tornos, 2009; Chen et al., 2010). With increasing oxygen fugacity, driven by cooling in a sulphate environment, hematite becomes stable. Hematite plus K-feldspar and sericite alteration are expected to form at ~ 100-300°C with Cu+Fe sulphide deposition at the contact with carbonate-rich metasediments.

A lateral zonation in oxide alteration is observed in the Mumbwa district with a magnetite core zone characteristic of the central area (Mutoya s.s. and Mushingashi) together with potassic and potassic-calcic alteration, while to the south (Kitumba) hematite + K-feldspar + sericite and chlorite alteration prevail, and to the extreme north of Mutoya (Worm) hematite and manganosiderite dominate.

According to Barton (2014), in IOCG systems Na-Ca assemblages tend to be peripheral, deep and barren, and Duncan et al. (2011, 2014) show that in many IOCG deposits in the Cloncurry district, sodic-calcic alteration occurs at a regional scale, becoming a diagnostic precursor to mineralization, as it drives the release of base and precious metals. However, scapolite development has been only locally been reported in the Mumbwa district, associated with granitoids, as an accessory phase in syenites along fault zones, in calc-silicate, or in skarn (Abell, 1970, 1976; Cikin and Drysdall, 1971; Page, 1974; Griffiths, 1998; Seifert, 2000), but no sectors of the Hook area with significant zones of pervasive Na alteration have been documented. This suggests that either a sodic alteration is not exposed, or that hydrothermal potassic alteration may have replaced an older (and perhaps not pervasive) Na or Na(-Ca) alteration phase. This could be the case, for example, in the Olympic Dam district, where it is suggested that early Na-alteration has been extensively replaced by K-feldspar (Bastrakov et al., 2007), or at NICO and Sue-Diann (NW Territories, Canada), where the sodic alteration is missing or not exposed, and the only distal alteration is potassic (e.g., Goad et al., 2000).

As to the supergene alteration observed at Kitumba, it is possible that multiple events acted at different times. This conclusion is supported by the presence of native copper and pseudomalachite, as well as by the multiple depth levels where secondary copper mineralization has been intersected (for example, at least three different supergene intervals are recorded in borehole S36_1). Hitzman (pers. comm., 2008) suggested that, in the Mumbwa hematite breccias, acidic solutions derived from weathering were able to deeply penetrate the rocks because of the relatively small amounts of acid-consuming materials

such as wall-rock clasts and carbonates to neutralize the circulating acidic. Indeed, Cu leaching and re-concentration appears minor in K-feldspar- and carbonate-rich alteration assemblages, which carry a strong acid-buffering capacity.

In the 22 analyzed rocks we can distinguish 3 major alteration-types: a) rocks affected by potassic alteration (S1_1/0, S1_1/1, S1_1/2, S36_1/4, S36_1/5, S36_33/6, S36_33/7A, MUM4D/7. MUM6BD/4); b) rocks exhibiting sericite-chlorite alteration (Mg-Fe-enriched) superimposed on K-enrichment (S1_1/4, S36_1/8, S36_1/12, S36_33/11, S36_33/15); c) magnetite-rich rocks characterized by calc-silicate alteration (mostly epidote), corresponding to the samples from the Mutoya centre. Exceptions are the K-altered samples MUM4D/7 and MUM6BD/4.

Fig. 13 includes all samples of igneous and metasedimentary rocks, as it helps in visualizing the effects on SiO_2, CaO, FeO, MgO induced by the alteration in comparison with the inferred granite and syenite protoliths. Both Fig. 13A and B were originally developed for volcanic-hosted massive sulphide (VHMS) deposits, but they have been also used to discriminate between different polymetallic systems, including IOCGs (e.g., Corriveau et al., 2017).

Figure 13A plots the alteration index (AI) of Ishikawa et al. (1976) vs. the chlorite-carbonate-pyrite index (CCPI) of Large et al. (2001) and discriminates between the three alteration types. Compared to the field of ‘least altered rocks’, K-altered samples (in yellow) show a shift towards higher AI values at a relatively constant CCPI index (excluding the Fe-rich sample S36_33/7A), indicating that the potassic alteration was paired with CaO and Na_2O removal. The mineralized samples contain hypogene sulphides, and are sericite-chlorite altered (grey circles in Fig. 13, S36_1/8, S36_1/12, S36_33/11, S36_33/15). These samples are Fe-Mg-rich, and plot with high AI and high-CCPI, as sericite-chlorite and sulphides overprint the potassic alteration. Group c samples (in green in Fig. 13) contain calc-silicate phases; these rocks are CCPI-enriched, while their AI index is commonly similar to the protoliths.

A clear distinction between calc-silicate and non-calc-silicate phases is also apparent when plotting the AI vs. the advanced argillic alteration index (AAAI) of Williams and Davidson (2004) (Fig. 13B), as both indices are influenced by the CaO content of the samples, while Na_2O is invariably negligible.

The A’KF ternary phase diagram of Bonnet and Corriveau (2007) in Fig. 13C further emphasizes the departure from the syenite or granite precursors towards K-altered but Cu-unmineralized rocks, or towards variably Fe-Mg-Mn-rich products, which include Fe-oxidized + chlorite-rich and Fe-oxidized + Ca-Mg-rich rocks. The Cu-mineralized rocks of the Kitumba anomaly also converge towards this part of the diagram. In the phase diagram CKS (Fig. 13D), alteration vectors discriminate the samples affected by silicification (highest silica in

S36_1/4, S36_33/6, S36_33/7A) from the variably altered (potassic ± chlorite) rocks (also including the copper-rich ones) and from the Ca-Mg-altered samples of Mutoya s.s and Mushingashi (in green).

The diagrams constrain an interaction between alteration and mineralization, as the high-Cu mineralized Kitumba samples are sericite-chlorite-rich. This can be explained by remembering that sericite (+ chlorite + carbonate) alteration is often recorded towards the eastern margins of the syenitic intrusive system. This happens preferentially at lineament intersections and closer to the Kitumba Fault Zone, in association with hematite breccias which acted as preferential outflow for the hydrothermal CO_2-rich fluids and hematite + sulphide growth. An inferred high CO_2 content in the magmatic fluids is indicated by the abundance of carbonate phases. K-feldspar hydrolyzation and sericite development would be triggered by the production of carbonic acid (due to H_2O-CO_2 interaction), with pH lowering and transition to hematite-dominated conditions.

5.4. Affinities with known IOCG localities worldwide

Field and laboratory observations, combined with geochemical analyses of mineralized-unmineralized cores show that, among the world-class IOCG deposits, similarities exist between the Mumbwa district deposits and the large-scale IOCG deposit of Candelaria (Chile, Marschik and Fontboté, 2001). Both developed in orogenic settings in association with coeval igneous rocks (although with calc-alkaline affinity at Candelaria); they include skarn and/or calc-potassic alteration and strong potassic metasomatism, and mineralization has likely been derived from a hybrid hydrothermal system under relatively oxidized conditions (hematite-dominated). The transition from high-T magnetite-rich to a lower-T hematite-dominated environment, as seen in the studied prospects, is typical of several IOCG deposits in the Andes, including Mantoverde (Tornos et al., 2010), and at the Olympic Dam deposit (Gawler craton, e.g., Williams et al., 2005), but in North American IOCG systems, it is also inferred that such zonation reflects the evolution from a deep IOA to a shallower IOCG system (Montreuil et al., 2013; Corriveau et al., 2016). Brecciation and hydrothermal alteration assemblages developed along the N-S-to NNW-SSE-trending structural corridor of the Mumbwa Fault Zone, sharing similarities with Olympic Dam (Skirrow et al., 2007) and with the Mount Isa Inlier, Cloncurry district in Australia (Duncan et al., 2014).

In terms of host rocks, A-type intrusive units, like the Hook granitoids, can be considered a valid exploration tool, because they are often associated with IOCG systems (Corriveau, 2007; Corriveau et al., 2017). Magmatic suites with chemistry comparable to the Hook batholith (predominantly metaluminous, magnetite-bearing alkaline to subalkaline, K-rich)

characterize the Mesoproterozoic intrusions of the Williams and Naraku batholiths of the Ernest Henry IOCG system, Cloncurry district (Mark et al., 2006), the Palaeoproterozoic intrusive Hiltaba Suite at Olympic Dam, Gawler craton (Skirrow et al., 2007), and can also be found in the Amazon craton (Archean Salobo deposit; e.g., Giles, 1988; Creaser, 1996; Requia et al., 2003) and in the Canadian Shield (Palaeoproterozoic Eden Lake Complex, Manitoba; Palaeoproterozoic to Mesoproterozoic Central Mineral belt, Labrador, e.g., Corriveau, 2007).

6. Conclusions

Since modern exploration started in the 1990s, two large hydrothermal centres have been identified in the Mumbwa district (the southern Sugar Loaf and northern Mutoya), characterized by a strong magnetic and gravimetric signal along an approximately 1 km wide, 25-km-long, NW-SE to N-S-trending structural corridor. The systems are centreed on, and follow, a series of intrusive syenitic bodies inferred to belong to the latest phase of the Pan-African Hook batholith. A massive magnetite replacement at the Mutoya centre is flanked in its northernmost part and to the south (Sugar Loaf centre) by hematite-rich hydrothermal breccias, mineralized veins and stockwork. Brecciation was likely to have been triggered by exsolution of magmatic volatiles and possible mixing with evaporitic/meteoric fluids circulating along structural pathways.

The Kitumba prospect (Sugar Loaf centre) is presently the main focus of exploration. At Kitumba, copper mineralization is characterized by a disseminated to massive primary chalcopyrite assemblage with minor bornite and chalcocite, and subsequently modified by deep weathering and oxidation. This resulted in a redistributed supergene mineralization comprising secondary copper minerals such as malachite, chalcocite, copper phosphates, cuprite, covellite, digenite, chrysocolla, and bornite, as well as native copper. Supergene alteration occurs in some boreholes to depths exceeding 700 m. The pervasive zonation in alteration, from magnetite (± apatite, amphibole), to K-feldspar, carbonate, hematite, and sericite ± chlorite testifies to the transition to lower temperature and higher oxygen fugacity at shallower depths.

Interaction between low-T hydrothermal fluids of magmatic origin and cooler/oxidized non-magmatic fluids is inferred. Macro and microscopic observations, geochemistry and isotopes suggest that sulphur was likely to have been sourced from a combination of magmatic fluids and evaporitic brines.

Replacement of pyrite by chalcopyrite in breccias and veins is recorded to increase towards the eastern margin of Kitumba, where hematite and fracture-induced permeability become predominant along the Kitumba Fault Zone. Interaction of magmatic volatiles (H_2O and CO_2)

with cooler basinal (± meteoric) components along the fault system was likely to have been the main mechanism for chalcopyrite deposition.
Most of the IOCG system features are verified, but the scarce Au content and high Fe/Cu sulphide distribution mitigate against an unambiguous classification. We also suggest that the high magnetite-pyrite zones prevailing at depth and at the margins of the system are more akin to a Kiruna type root, on top of which the remnants of an IOCG mineralized system - at Kitumba and in other Cu-rich areas like Kakozhi - are preserved.

Acknowledgements

This work is part of a two year collaborative research project involving the University of the Witwatersrand and RioTinto Exploration Ltd., in an attempt to correlate the Damara Belt in Namibia with the Lufilian Arc and Zambezi belt in Zambia. Murray Hitzman, Simone Runyon, John Slack and John Thompson are gratefully thanked for the detailed revision of an earlier version of this article. Akalemwa Kamona (University of Namibia) and an anonymous reviewer contributed with precious suggestions to the final version of the paper. Rio Tinto is acknowledged for useful discussion as well as financial contribution to analytical work and fieldtrips. Blackthorn Resources Ltd., Intrepid Mines Ltd. and MSA Group kindly provided the studied sample rocks from the drillcore yard of the Mumbwa exploration camp, as well as logistic and technical assistance to LM, JL, KN, KS, PN and JK. We thank Mike Robertson (MSA Group), who contributed significantly to the improvement of the manuscript, as well as Adam Engela and Katie Hill (Wits University), for separating sulphides and undertaking sulphur isotope analysis. The iThemba Labs at the University of the Witwatersrand kindly provided equipment and assistance for the isotopic study. We acknowledge South African THRIP for research funding (Project ID: TP2010072800046 to Judith Kinnaird) and CIMERA for NRF-DST for supporting further analytical data.

References

Abell, R.S., 1970, The geology of the Nansenga River area. Explanation of Degree Sheet 1526, NE Quarter: Report of the Geological Survey of Zambia, v. 25, 65 p.

Abell, R.S., 1976, The geology of the Lukomezi River area. Explanation of Degree Sheet 1526, NW Quarter: Report of the Geological Survey of Zambia, v. 33, 34 p.

Annels, A.E., 1974, Some aspects of the stratiform ore deposits of the Zambian Copperbelt and their genetic significance, in: Bartholomé , P., ed., Gisements stratiformes et provinces cupifères. Liège, Société Géologique Belgique, p. 235–254.

Baker, T., Perkins, C., Blake, K.L., and Williams, P.J. 2001, Radiogenic and stable isotope constraints on the genesis of the Eloise Cu–Au deposit, Cloncurry district, northwest Queensland: Economic Geology, v. 96, p. 723-742.

Barra, F., Reich, M., Selby, D., Rojas, P., Simon, A.C., Salazar, E., and Palma, G., 2017, Unraveling the origin of the Andean IOCG clan: A Re-Os isotopes approach: Ore Geology Reviews, v. 81, p. 62-78.

Barton, M.D., 2014, Iron Oxide(-Cu-Au-REE-P-Ag-U-Co) Systems, in: Holland, H., and Turekian, K., eds., Treatise on Geochemistry 2nd Edition, 13, p. 515-541.

Barton, M.D. and Johnson, D.A., 2004, Footprints of Fe-oxide(-Cu-Au) systems. SEG 2004: Predictive Mineral Discovery Under Cover. Centre for Global Metallogeny, Spec. Pub. 33, The University of Western Australia, p. 112-116.

Barton, M.D. and Johnson, D.A., 2000, Alternative brine sources for Fe-oxide (Cu–Au) systems: Implications for hydrothermal alteration and metals. in: Porter, T.M., ed., Hydrothermal Iron Oxide Copper–Gold and Related Deposits: A Global Perspective, Glenside, SA, Australian Mineral Foundation, p. 43-60.

Barton, M.D., and Johnson, D.A., 1996, Evaporitic source model for igneous related Fe oxide-(REE-Cu-Au-Au) mineralization: Geology, v. 24, p. 259–262.

Bastrakov, E.N., Skirrow, R.G., and Davidson, G.J., 2007, Fluid evolution and origins of iron oxide Cu-Au prospects in the Olympic Dam district, Gawler Craton, South Australia: Economic Geology, v. 102, p. 1415-1440.

Belperio, A., Flint, R., and Freeman, H., 2007, Prominent Hill: a hematite-dominated, iron oxide copper-gold system: Economic Geology, v. 102, p. 1499-1510.

Binda, P.L., 1994, Stratigraphy of the Zambian Copperbelt orebody: Journal of African Earth Sciences, v. 19, p. 251–264.

Blackthorn Resources Limited, 2014, Annual report, 85 p. http://www.blackthornresources.com.au/uploads/documents/ASX%20ANN_2014%20Annual%20Report_20140926.pdf

Blevin, P.L., and Chappell, B.W., 1992, The role of magma sources, oxidation states and fractionation in determining the granite metallogeny of eastern Australia: Transactions of the Royal Society of Edinburgh, v. 83, p. 305–316.

Bonnet, A-L., and Corriveau, L., 2007, Alteration vectors to metamorphosed hydrothermal systems in gneissic terranes, in: Goodfellow, W.D., ed., Mineral Deposits of Canada: A Synthesis of Major Deposit-Types, District Metallogeny, the Evolution of Geological Provinces, and Exploration Methods: Geological Association of Canada, Mineral Deposits Division, Special Publication No. 5, p. 1035-1049.

Bonnet, A-L., Corriveau, L., and La Flèche, M.R., 2005, Chemical imprint of highly metamorphosed volcanic-hosted hydrothermal alterations in the La Romaine

Supracrustal Belt, eastern Grenville Province, Quebec: Canadian Journal of Earth Sciences, v. 42, p. 1783–1814.

Boynton, W.V., 1985, Cosmochemistry of the rare earth elements: meteorite studies, in: Henderson, P., ed., Rare Earth Element Geochemistry. Developments in Geochemistry 2. Elsevier, Amsterdam, p. 115–152.

Broman, C., Nystrom, J.O., Henriquez, F., and Elfman, M., 1999, Fluid inclusions in magnetite–apatite ore from a cooling magmatic system at El Laco, Chile: GFF, v. 121, p. 253–267.

Brooks, E., White, J.W.C., Schilla, A., Bender, M., Barnett, B.A., Serveringhaus, J., Taylor, K.C., Alley, R.B., Steig, E.J., 2005, Timing of millennial-scale climate change at Siple Dome, West Antarctica, during the last glacial period: Quaternary Science Reviews, v. 24, p. 1333-1343.

Bull, S., Selley, D., Broughton, D., Hitzman, M., Cailteux, J., Large, R., and McGoldrick, P., 2011, Sequence and carbon isotopic stratigraphy of the Neoproterozoic Roan Group strata of the Zambian copperbelt: Precambrian Research, v. 190, p. 70-89.

Candela, P.A., 1989, Felsic magmas, volatiles, and metallogenesis, in Whitney, J.A., Naldrett, A.J., eds., Ore deposition associated with magmas: Society of Economic Geology. Reviews in Economic Geology, v. 4, p. 223–233.

Chen, H.Y., 2010, Mesozoic IOCG mineralization in the central Andes: An updated review, in: Porter, T.M. ed., Hydrothermal Iron Oxide Copper–Gold and Related Deposits: A Global Perspective – Advances in the Understanding of IOCG Deposits, v. 3, p. 259–272. Adelaide: PGC Publishing.

Chen, H.Y., Clark, A.H., and Kyser, T.K., 2010, The Marcona magnetite deposit, Ica, central-south Peru: A product of hydrous, iron oxide-rich melt: Economic Geology, v. 105, p. 1441–1456.

Christensen, A., Whiting, T., 2013. The Role Of Falcon® Agg in the Mumbwa, Zambia, Iron Oxide Copper-gold discovery. 13th SAGA Biennial Conference & Exhibition, 10 p.

Chou, I-M., and Eugster, H.P., 1977, Solubility of magnetite in supercritical chloride solutions: American Journal of Science, v. 277, p. 1296-1314.

Cikin, M., 1972, Geology of the north-eastern margin of the Hook Granite Massif, Central Province: Report of the Geological Survey of Zambia, v. 12, p. 43-54.

Cikin, M., and Drysdall, A.R., 1971, The geology of the country north-west of Mumbwa (the Big Concession). Explanation of Degree Sheet 1426, SE Quarter: Report of the Geological Survey of Zambia, v. 27, 72 p.

Corriveau, L., 2007, Iron Oxide Copper-Gold (±Ag±Nb±P±REE±U) Deposits: A Canadian Perspective, in: Godfellow, W.D., ed., Mineral Deposits of Canada: A synthesis of major

deposit types, district metallogeny, the evolution of geological provinces, and exploration methods: Geological Association of Canada, p. 307-328.

Corriveau, L., Potter, E.G., Acosta-Gongora, P., Blein, O., Montreuil, J-F., De Toni, A.F., Day, W.C., Slack, J.F., Ayuso, R.A., Hanes, R., 2017, Petrological Mapping and Chemical Discrimination of Alteration Facies as Vectors to IOA, IOCG, and Affiliated Deposits within Laurentia and Beyond: SGA Québec 2017, Québec, Canada.

Corriveau, L., Montreuil, J-F., Potter, E.G., 2016, Alteration facies linkages among IOCG, IOA, and affiliated deposits in the Great Bear magmatic zone, Canada: Economic Geology, v. 111, p. 2045-2072.

Creaser, R.A., 1996, Petrogenesis of a Mesoproterozoic quartz latite granitoid suite from the Roxby Downs area, South Australia: Precambrian Research, v. 79, p. 371-394.

Day, W.C., Slack, J.F., Ayuso, R.A., and Seeger, C.M., 2016, Regional geologic and petrologic framework for iron oxide ± apatite ± rare earth element and iron oxide copper-gold deposits of the Mesoproterozoic St. Francois Mountains terrane, southeast Missouri, USA: Economic Geology, v. 111, p. 1825–1858.

de Swardt, A.M.J., and Drysdall, A.R., 1964, Precambrian geology and structure in central Northern Rhodesia: Memoir of the Geological Survey of Northern Rhodesia, v. 2.

De Haller, A., and Fontboté, L., 2009, The Raúl-Condestable iron oxide copper-gold deposit, central coast of Peru: Ore and related hydrothermal alteration, sulfur isotopes, and thermodynamic constraints: Economic Geology, v. 104, p. 365–384.

Dransfield, M.H., and Christensen, A.N., 2013, Performance of airborne gravity gradiometers: The Leading Edge, 32, 908–922.

Duncan, R.J., Stein, H.J., Evans, K.A., Hitzman, M.W., Nelson, E.P., and Kirwin, D.J., 2011, A New Geochronological Framework for Mineralization and Alteration in the Selwyn-Mount Dore Corridor, Eastern Fold Belt, Mount Isa Inlier, Australia: Genetic Implications for Iron Oxide Copper-Gold Deposits: Economic Geology, v. 106, p. 169-192.

Duncan, R.J., Hitzman, M.W., Nelson, E.P., and Togtokhbayar, O., 2014, Structural and lithological controls on iron oxide copper gold deposits of the southern Selwyn-Mount Dore corridor, eastern fold belt, Queensland, Australia: Economic Geology, v. 109, p. 419-456.

Edfelt, A., and Martinsson, O., 2003, The Tjarrojakka Fe-oxide Cu (-Au) occurrence, Kiruna area, northern Sweden, in Eliopoulos, D.G., et al. eds., Mineral Exploration and Sustainable Development. Millpress, Rotterdam, p. 1069-1072.

Ehrig, K., McPhie, J. and Kamenetsky, V., 2013, Geology and mineralogical zonation of the Olympic Dam iron oxide Cu-U-Au-Ag deposit, South Australia, in Hedenquist, J.W., Harris W., Camus, F., eds., Geology and genesis of major copper deposits and districts

of the world: a tribute to Richard H. Sillitoe, Special Publication 16: Society of Economic Geologists, p. 237–268.

Frimmel, H.E., Basei, M.S., and Gaucher, C., 2011, Neoproterozoic geodynamic evolution of SW-Gondwana: a southern African perspective: International Journal of Earth Sciences (Geol Rundsch), v. 100, p. 323–354.

Giles, C.W., 1988, Petrogenesis of the Proterozoic Gawler Range volcanics, South Australia: Precambrian Research, v. 40/41, p. 407-427.

Goad, R.E., Mumin, A.H., Duke, N.A., Neale, K.L., Mulligan, D.L., and Camier, J.W., 2000, The NICO and Sue-Dianne Proterozoic, Iron Oxide-hosted, Polymetallic Deposits, Northwest Territories: Application of the Olympic Dam Model in Exploration: Exploration and Mining Geology, v. 9, p. 123-140.

Goscombe, B.D., Armstrong, R. and Barton, J.M., 2000, Geology of the Chewore Inliers: Constraining the Mesoproterozoic to Palaeozoic evolution of the Zambezi Belt. Journal of African Earth Sciences, v. 30, p. 589-627.

Gow, P.A., Wall, V.J., Oliver, N.H.S., and Valenta, R.K., 1994, Proterozoic iron oxide (Cu-U-Au-REE) deposits: Further evidence of hydrothermal origins: Geology, v. 22, p. 633-636.

Grainger, C.J., Groves, D.I., Tallarico, F.H.B., and Fletcher, I.R., 2008, Metallogenesis of the Carajás mineral province, southern Amazon craton, Brazil: Varying styles of Archean through Paleoproterozoic to Neoproterozoic base-and precious-metal mineralisation: Ore Geology Reviews, v. 33 p. 451–489.

Grant, J.A., 1986, The Isocon diagram-a simple solution to Gresens' equation for metasomatic alteration: Economic Geology, v. 81, p. 1976-1982.

Gray, D.R., Foster, D.A., Meert, J.G., Goscombe, B.D., Armstrong, A., Trouw, R.A.J., and Passchier, C.W., 2008, A Damara orogen perspective on the assembly of southwestern Gondwana, in Pankhurst, R.J., Trouw, R.A.J., Brito Neves, B., and De Wit, M.J. eds., West Gondwana: Pre-Cenozoic Correlations Across the South Atlantic Region: Geological Society, London, Special Publications, v. 294, p. 257–278.

Griffiths, C.M., 1998, Geology of the Ngoma, Namwala and Mala areas. Explanation of Degree Sheet 1525, SE Quarter and 1526, SW & SE Quarters: Report of the Geological Survey of Zambia, v. 77, 66 p.

Groves, D.I., and Vielreicher, N.M., 2001, The Phalaborwa carbonatite-hosted magnetite-copper sulphide deposit, South Africa: an end-member of the iron-oxide copper-gold-rare element deposit group?: Mineralium Deposita, v. 36, p. 89–194.

Groves, D.I., Bierlein, F.P., Meinert, L.D., and Hitzman, M.W., 2010, Iron Oxide Copper-Gold (IOCG) Deposits through Earth History: Implications for Origin, Lithospheric Setting, and Distinction from Other Epigenetic Iron Oxide Deposits: Economic Geology, v. 105, p. 641-654.

Hanson, R.E., Wardlaw, M.S., Wilson, T.J., and Mwale, G., 1993, U-Pb zircon ages from the Hook granite massif and Mwembeshi dislocation: Constraints on Pan-African deformation, plutonism, and transcurrent shearing in central Zambia: Precambrian Research, v. 63, p. 189-209.

Hanson, R.E., Wilson, T.J., and Munyanyiwa, H., 1994, Geologic evolution of the Neoproterozoic Zambezi Orogenic Belt in Zambia: Journal of African Earth Sciences, v. 18, p. 135-150.

Hargrove, U.S., Hanson, R.E., Martin, M.W., Blenkinsop, T.G., Bowring, S.A., Walker, N., and Munyanyiwa, H., 2003. Tectonic evolution of the Zambezi belt: Geochronological, structural and petrographical constraints from Northern Zimbabwe. Precambrian Research, v. 123, p. 159–186.

Hayes, T.S., Landis, G.P., Whelan, J.F., Rye, R.O., and Moscati, R.J., 2012, The Spar Lake strata-bound Cu-Ag deposit formed across a mixing zone between trapped natural gas and metal-bearing brine: Economic Geology, v. 107, p. 1223-1250.

Haywood, N., 2008, The geodynamic setting and magmatic controls on genesis of world-class IOCG ore deposits: Geological Society of Australia, Abstracts, v. 89, p. 130.

Hemley, J.J., Cygan, G.L., Fein, J.B., Robinson, G.R., and D'Angelo, W.M, 1992, Hydrothermal ore-forming processes in the light of studies in rock buffered systems: 1. iron-copper-zinc-lead sulphide solubility relations: Economic Geology, v. 87, p. 1-22.

Hitzman, M.W., 2000, Iron oxide–Cu–Au deposits. What, where, when and why, in: Porter TM ed., Hydrothermal Iron Oxide Copper-Gold and Related Deposits: A Global Perspective: AMF, Adelaide, p. 9-26.

Hitzman, M.W., Oreskes, N., and Einaudi, M.T., 1992, Geological characteristics and tectonic setting of Proterozoic iron oxide (Cu-U-Au-REE) deposits: Precambrian Research, v. 58, p. 241-287.

Hoy, L.D., and Ohmoto, H., 1989, Constraints for the genesis of redbed-associated stratiform Cu deposits from sulphur and carbon mass-balance relations, in Boyle, R.W., Brown, A.C., Jefferson, C.W., Jowett, E.C., and Kirkham, R.V. eds., Sediment-hosted stratiform copper deposits: Geological Association of Canada Special Paper, v. 36, p. 135–149.

Hunt, J.A., Baker, T., and Thorkelson, D.J., 2007, A review of iron oxide copper–gold deposits, with focus on the Wernecke Breccias, Yukon, Canada, as an example of a non-magmatic end member and implications for IOCG genesis and classification: Exploration and Mining Geology, v. 16, p. 209-232.

Intrepid Mines Limited, 2015, Kitumba Project – updated PFS results and reserves, 32p, https://www.asx.com.au/asxpdf/20151008/pdf/431xvpyn6qmsj9.pdf.

Intrepid Mines Limited, 2017, Annual report for the year ended 31 December 2017, 56 p., http://www.annualreports.com/Company/intrepid-mines-ltd.

Ishikawa, Y., Sawaguchi, T., Iwaya, S., and Horiuchi, M., 1976, Delineation of prospecting targets for Kuroko deposits based on modes of volcanism of underlying dacite and alteration halos: Mining Geology, v. 26, p. 105–117.

John, T., and Schenk, V., 2003, Partial eclogitisation of gabbroic rocks in a late Precambrian subduction zone (Zambia): prograde metamorphism triggered by fluid infiltration: Contributions to Mineralogy and Petrology, v. 146, p. 174-191.

John, T., Schenk, V., Haase, K., Scherer, E., and Tembo, F., 2003, Evidence for a Neoproterozoic ocean in south-central Africa from mid-oceanic-ridge-type geochemical signatures and pressure-temperature estimates of Zambian eclogites: Geology, v. 31, p. 243-246.

John, T., Schenk, V., Mezger, K., and Tembo, F., 2004a, Timing and PT evolution of whiteschist metamorphism in the Lufilian Arc–Zambezi Belt Orogen (Zambia): implications for the assembly of Gondwana: Journal of Geology, v. 112, p. 71–90.

John, T., Scherer, E.E., Haase, K., and Schenk, V., 2004b, Trace element fractionation during fluid-induced eclogitization in a subducting slab: trace element and Lu-Hf-Sm-Nd isotope systematics: Earth and Planetary Science Letters, v. 227, p. 441-456.

Johnson, J.P., and McCulloch, M.T., 1995, Sources of mineralizing fluids for the Olympic Dam deposit, (South Australia): Sm-Nd isotopic constraints: Chemical Geology, v. 121, p. 177-199.

Johnson, S.P., Rivers, T., and De Waele, B., 2005, A review of the Mesoproterozoic to early Palaeozoic magmatic and tectonothermal history of south-central Africa: implications for Rodinia and Gondwana. Journal of the Geological Society of London, v. 162, p. 433-450.

Johnson, S.P., De Waele, B., Evans, D., Banda, W., Tembo, F., Milton, J.A., and Tani, K., 2007, Geochronology of the Zambezi supracrustal sequence, southern Zambia: a record of Neoproterozoic divergent processes along the southern margin of the Congo Craton: Journal of Geology, v. 115, p. 355-374.

Kampunzu, A.B., Tembo, F., Matheis, G., Kapenda, D., and Huntsman-Mapila, P., 2000, Geochemistry and tectonic setting of mafic igneous units in the Neoproterozoic Katangan Basin, Central Africa: implications for Rodinia break-up: Gondwana Research, v. 3, p. 125-153.

Knipping, J.L., Bilenker, L.D., Simon, A.C., Reich, M., Barra, F., Deditius, A.P., Lundstrom, C., Bindeman, I., and Munizaga, R., 2015, Giant Kirunatype deposits form by efficient flotation of magmatic magnetite suspensions: Geology, v. 43, p. 591–594.

Large, R.R, Gemmell, J.B., Paulick, H., and Huston, D.L., 2001, The Alteration Box Plot: A Simple Approach to Understanding the Relationship between Alteration Mineralogy and

Lithogeochemistry Associated with Volcanic-Hosted Massive Sulfide Deposits: Economic Geology, v. 96, p. 957-971.

Lee, J.B., 2001, FALCON Gravity Gradiometer Technology, Exploration Geophysics, 32, p. 75-79.

Lehmann, B., 1990, Metallogeny of tin: Lecture notes in Earth Sciences. Springer, Berlin Heidelberg New York, 211 p.

Mao, M., Rukhlov, A.S., Rowins, S.M., Spence, J., and Coogan, L., 2016, Apatite Trace Element Compositions: A Robust New Tool for Mineral Exploration: Economic Geology, v. 111, p. 1187–1222.

Mark, G., Oliver, N.H.S., Williams, P.J., Valenta, R.K., and Crookes, R.A., 2000, The evolution of the Ernest Henry Fe-oxide-(Cu–Au) hydrothermal system, in: Porter, T.M., ed., Hydrothermal iron oxide copper–gold and related deposits: a global perspective: Australian Mineral Foundation, Adelaide, p. 123–136.

Mark, G., Oliver, N.H.S., and Williams, P.J., 2006, Mineralogical and chemical evolution of the Ernest Henry Fe oxide–Cu–Au ore system, Cloncurry district, northwest Queensland, Australia: Mineralium Deposita, v. 40, p. 769-801.

Marschik, R., and Fontboté, L., 1996, Copper(-iron) mineralization and superposition of alteration events in the Punta del Cobre belt, northern Chile: Society of Economic Geologists Special Publication, v. 5, p. 171–189.

Marschik, R., and Fontboté, L., 2001, The Candelaria-Punta del Cobre Iron Oxide Cu–Au (–Zn–Ag) deposits, Chile: Economic Geology, v. 96, p. 1799-1826.

Mathur, R.D., Marschik, R., Ruiz, J., Munizaga, F., Leveille, R.A., and Martin, W., 2002, Age of mineralization of the Candelaria iron oxide Cu-Au deposit and the origin of the Chilean iron belt based on Re-Os isotopes: Economic Geology, v. 97, p. 59–71.

McPhail, D.C., 1993, The behavior of iron in high temperature chloride brines: Geological Society of Australia Abstracts Series, v. 34, p. 50-51.

Milani, L., Lehmann, J., Naydenov, K., Kinnaird, J.A., Saalmann, K., Daly, S., Frei, D., and Lobo-Guerrero Sanz., A., 2015, A-type magmatism in a syn-collisional setting: the case of the Pan-African Hook Batholith in Central Zambia: Lithos, v. 216, p. 48-72.

Miller, R.McG., 2008, The geology of Namibia: Neoproterozoic to Lower Paleozoic, in: Miller, R.McG. ed., The Geology of Namibia vol. 2: Namibian Geological Survey, Windhoek, Namibia.

Montreuil, J.-F., Corriveau, L., and Grunsky, E.C., 2013, Compositional data analysis of hydrothermal alteration in IOCG systems, Great Bear magmatic zone, Canada: to each alteration type its own geochemical signature: Geochemistry: Exploration, Environment, Analysis 2013, v.13, p. 229-247.

Naydenov, K.V., Lehmann, J., Saalmann, K., Milani, L., Kinnaird, J.A., Charlesworth, G., Frei, D., and Rankin, W., 2014, New constraints on the Pan-African Orogeny in Central Zambia: structural and geochronological study of the Hook Batholith and the Mwembeshi Zone: Tectonophysics, v. 637, p. 80-105.

Naydenov, K.V., Lehmann, J., Saalmann, K., Milani, L., Poterai, J., Kinnaird, J.A., Charlesworth, G., and Kramers, J.D., 2016, The geology of the Matala Dome: an important piece of the Pan-African puzzle in Central Zambia: International Journal of Earth Sciences, v. 105, p. 695-712.

Ohmoto, H., and Rye, R.O., 1979, Isotopes of sulfur and carbon, in: Barnes, H.L., ed., Geochemistry of Hydrothermal Ore Deposits, 2nd ed., New York: Wiley, p. 509–567.

Oreskes, N., and Einaudi, M.T., 1992, Origin of Hydrothermal Fluids at Olympic Dam: Preliminary Results from Fluid Inclusions and Stable Isotopes: Economic Geology, v. 87, p. 64-90.

Page, T.C., 1974, Geology of the Lubungu and Lungu areas: Explanation of Degree Sheet 1426, NW & SW Quarters: Report of the Geological Survey of Zambia, v. 39, 23 p.

Phillips, K.A., 1965, Geology of the Luiri Hill area: Explanation of Degree Sheet 1527, NW Quarter: Report Geological Survey of Zambia, v. 4, 69 p.

Phillips, K.A., and Newton, A.R., 1956, A summary of the Katanga succession in the Mumbwa area with a supplement on the igneous rocks of the area: Occasional Paper of the Geological Survey of Northern Rhodesia, v. 10, Supplement 4-5, 12 p.

Pipping, F., 1975, The geology of the Mutapanda River area. Explanation of Degree Sheet 1426, NE Quarter. Report of the Geological Survey of Zambia, v. 31, 20 p.

Pollard, P.J., 2006, An intrusion-related origin for Cu–Au mineralization in iron oxide–copper–gold (IOCG) provinces: Mineralium Deposita, v. 41, p. 179-187.

Porada, H., 1989, Pan-African rifting and orogenesis in Southern to Equatorial Africa and Eastern Brazil: Precambrian Research, v. 44, p. 103–136.

Porada, H., and Berhorst, V., 2000, Towards a new understanding of the Neoproterozoic-Early Palaeozoic Lufilian and northern Zambezi Belts in Zambia and the Democratic Republic of Congo: Journal of African Earth Sciences, v. 30, p. 727-771.

Rainaud, C., Master, S., Armstrong, R.A., Phillips, and D., Robb, L.J., 2005, Monazite U–Pb dating and 40Ar–39Ar thermochronology of metamorphic events in the Central African Copperbelt during the Pan-African Lufilian Orogeny: Journal of African Earth Sciences, v. 42, p. 183-199.

Requia, K., Stein, H., Fontboté, L., and Chiaradia, M., 2003, Re-Os and Pb-Pb geochronology of the Archean Salobo iron oxide copper-gold deposit, Carajas mineral province, northern Brazil: Mineralium Deposita, v. 38, p. 727-738.

Rieger, A.A., Marschik, R., Diaz, M., Holzl, S., Chiaradia, M., Akker, B., and Spangenberg, J.E., 2010, The hypogene iron oxide copper–gold mineralization in the Mantoverde District, Northern Chile: Economic Geology, v. 105, p. 1271-1299.

Robertson, M., 2013, Kitumba – a new kind of copper deposit in a Zambian context: The Southern African Institute of Mining and Metallurgy Base Metals Conference, 20 p.

Rotherham, J.R., Blake, K.L., Cartwright, I., and Williams, P.J. 1998, Stable isotope evidence for the origin of the Mesoproterozoic Starra Au–Cu deposit, Cloncurry district, northwest Queensland: Economic Geology, v. 93, p. 1435–1449.

Seal, R.R., 2006, Sulfur Isotope Geochemistry of Sulfide Minerals: Reviews in Mineralogy & Geochemistry, v. 61, p 633-677.

Seifert, A.V., 2000, Geology of the Chunga area. Explanation of degree sheet 1525. NE Quarter: Report Geological Survey of Zambia, v. 75, 23 p.

Selley, D., Broughton, D., Scott, R., Hitzman, M.W., Bull, S., Large, R., McGoldrick, P., Croaker, M., and Pollington, N., 2005, A new look at the geology of the Zambian Copperbelt: Society of Economic Geologists, 100th Anniversary Volume, p. 965–1000.

Sillitoe, R.H., 2003, Iron oxide-copper-gold deposits: An Andean view: Mineralium Deposita, v. 38, p. 787–812.

Simon, A.C., Knipping, J., Reich, M., Barra, F., Deditius, A.P., Bilenker, L., and Tristan Childress, T., 2018, Kiruna-Type Iron Oxide-Apatite (IOA) and Iron Oxide Copper-Gold (IOCG) Deposits Form by a Combination of Igneous and Magmatic-Hydrothermal Processes: Evidence from the Chilean Iron Belt: Society of Economic Geologists, Inc. SEG Special Publications, no. 21, pp. 89–114.

Skirrow, R.G., 2008, “Hematite-group” IOCG ± U ore systems: Tectonic settings, hydrothermal characteristics, and Cu-Au and U mineralizing processes, in Corriveau, L., Mumin, H., eds., Exploring for iron oxide copper-gold deposits: Canada and global analogues: GAC-MAC-SEGSGA-2008, Quebec City, May 29-30, Geological Association of Canada, Short Course Notes.

Skirrow, R.G., Bastrakov, E.N., Barovich K., Fraser, G.L., Creaser, R.A., Fanning, C.M., Raymond, O.L., and Davidson, G.J., 2007, Timing of Iron Oxide Cu-Au-(U) Hydrothermal Activity and Nd Isotope Constraints on Metal Sources in the Gawler Craton, South Australia: Economic Geology, v. 102, pp. 1441–1470.

Skirrow, R.G., Bastrakov, E.N., Davidson, G., Raymond, O., and Heithersay, P., 2002, Geological framework, distribution and controls of Fe-oxide Cu-Au deposits in the Gawler Craton. Part II. Alteration and mineralisation, in Porter, T.M., ed., Hydrothermal iron oxide copper-gold and related deposits, 2, PGC Publishing, Adelaide, p. 33-47.

Sverjensky, D.A., Hemley, J.J., and D'Angelo, W.M., 1991, Thermodynamic assessment of hydrothermal alkali feldspar-mica-aluminosilicate equilibria: Geochimica et Cosmochimica Acta, v. 55, p. 989-1004.

Tornos, F., Velasco, F., Barra, F., and Morata, D., 2010, The Tropezón Cu–Mo–(Au) deposit, Northern Chile: the missing link between IOCG and porphyry copper systems?: Mineralium Deposita, v. 45, p. 313-321.

Ullrich, T.D., and Clark, A.H., 1999, The Candelaria copper-gold deposit, Región III, Chile: Paragenesis, geochronology and fluid composition, in Stanley, C.J. et al., eds., Mineral deposits: Processes to processing: Rotterdam, Balkema, p. 201-204.

Unrug, R., 1988, Mineralization Controls and Source of Metals in the Lufilian Fold Belt, Shaba (Zaire), Zambia and Angola: Economic Geology, v. 83, p. 1247-1258.

Vajner, V., 1998, Geology of the country north-east of Mumbwa. Explanation of degree sheet 1427, SW Quarter: Report of the Geological Survey of Zambia, v. 29, 33 p.

Velasco, F., and Tornos, F., 2009, Pegmatite-like magnetite–apatite deposits of northern Chile: A place in the evolution of immiscible iron oxide melts? In Proceedings of the 10th Biennial SGA Meeting, Townsville, Australia: Society for Geology Applied to Ore Deposits, p. 665–667.

Vrána, S., Prasad, R., and Fediukova, E., 1975, Metamorphic kyanite eclogites in the Lufilian Arc of Zambia: Contributions to Mineralogy and Petrology, v. 51, p. 139-160.

Waller, C.G., Robertson, M.J., Witley, J.C., Carthew, G.H., and Morgan, D.J.Y., 2014, Kitumba copper project optimised pre-feasibility study: Intrepid Mines Ltd. NI 43-101 Technical Report, 279 p., https://www.miningdataonline.com/reports/ Kitumba_ PreFeasibility_Report_09252014.pdf

Whitney, J.A., Hemley, J.J., and Simon, F.O., 1985, The concentration of iron in chloride solutions equilibrated with synthetic granite compositions: The sulfur-free system: Economic Geology, v. 80, p. 444–460.

Williams, P.J., and Davidson, G.J., 2004, Possible submarine advanced argillitic alteration at the Basin Lake prospect, Western Tasmania, Australia; Economic Geology, v. 99, p. 987-1002.

Williams, P.J., and Pollard, P.J., 2003, Australian Proterozoic iron oxide– Cu–Au deposits: an overview with new metallogenic and exploration data from the Cloncurry district, northwest Queensland: Exploration and Mining Geology, v. 10, p. 191–213.

Williams, P.J., Barton, M.D., Johnson, D.A., Fontboté, L., de Haller, A., Mark, G., Oliver, N.H.S., and Marschik, R., 2005, Iron Oxide Copper-Gold Deposits: Geology, Space-Time Distribution, and Possible Modes of Origin: Economic Geology 100th Anniversary vol.. p. 371-405.

Woolrych, T.R.H., Christensen, A.N., McGill, D.L., and Whiting, T., 2015, Geophysical methods used in the discovery of the Kitumba iron oxide copper gold deposit. Interpretation: Special section: Mining and minerals exploration, v. 3, p. 15-25.

Zientek, M.L., Bliss, J.D., Broughton, D.W., Christie, M., Denning, P.D., Hayes, T.S., Hitzman, M.W., Horton, J.D., Frost-Killian, S., Jack, D.J., Master, S., Parks, H.L., Taylor, C.D., Wilson, A.B., Wintzer, N.E., and Woodhead J., 2014, Sediment-Hosted Stratabound Copper Assessment of the Neoproterozoic Roan Group, Central African Copperbelt, Katanga Basin, Democratic Republic of the Congo and Zambia: Scientific Investigations Report 2010–5090–T, USGS, 178 p.

Table captions

Table 1. Chemical composition and alteration/mineralization features of the Mumbwa cores (major elements in wt%, trace elements in ppm). Chemistry of inferred protoliths Z48 (syenite) and Z119A (granite) are included.

Table 2. Sulphur isotope values for sulphide minerals from the Mumbwa district. Cc=chalcocite; Ccp=chalcopyrite; Cu=native copper; Mal=malachite; Py=pyrite.

Table 3. Schematic representation of the temporal sequence of alteration phases at Kitumba. Note that coeval alterations do not always imply spatial association (e.g., carbonate-ankerite never occurs in hematite- and kaolinite-rich zones).

Table 4. Isocon analyses performed on qz-porphyry- and syenite-derived samples. Immobile elements and slopes obtained by linear regression are reported.

Figure captions

Fig. 1. Regional and local geological setting. A) Relationship between the Congo and Kalahari cratons and the main Pan-African mobile belts. B) Geological map of the Lufilian and Zambezi belts (modified after John et al., 2004a; Porada, 1989; Selley et al., 2005). C) Simplified geological map of the Hook batholith area (modified after Naydenov et al., 2014 and Milani et al., 2015). Sample location of Quartz-monzonite Z77 and inferred protoliths (Z48 - syenite, Z119A - granite) is shown; MwZ = Mwembeshi Zone.

Fig. 2. Geological map of the Mumbwa district (modified from the 1:100,000 scale geological map of Zambia - degree sheet 1426, SE quarter, Cikin and Drysdall, 1971), with historical

base-metal occurrences, main tectonic lineaments and location of studied drillcores. Boxes outline the Sugar Loaf and Mutoya mineralized centres.

Fig. 3. Representative data from the aerial Falcon survey over the Mumbwa area at 400 m line spacing. A) Total Magnetic Intensity – Reduced to the Pole (TMI RTP) with First Vertical Derivative (1VD) and Automatic Gain Control (AGC) filter. B) Uranium equivalent concentration. C) Airborne gravity gradient (AGG) Bouguer gravity-terrain corrected at 2.67 g/cm^3.

Fig. 4. Vertical gravity gradient (GDD) terrain corrected at 2.67 g/cm^3 over the Kitumba, southern Mutoya and Kakozhi prospects. The inferred lineaments are according to BHP Billiton structural interpretation.

Fig. 5. A) Lithological borehole logs from the studied drillcores from Kitumba and Mutoya (Mutoya s.s. and Mushingashi, courtesy of MSA group). Locations of all boreholes are shown in Fig. 2. Numbers to the left of the columns refer to labels of samples analyzed for element geochemistry and/or sulphur isotopes. Copper contents (in wt%) are also reported (maximum scales at 4 or 40 % Cu). B) Geological map of the Kitumba prospect with major lineaments and drill cores location (S1_1 out of map; modified after Waller et al., 2014). C) Interpretative geological section at Kitumba, drawn at ca. 8.373,900 mN, azimuth 183 on the basis of surface mapping and drill core interpolation (see also B) for location).

Fig. 6. Line drawing applied to the regional airborne geophysical survey defines boundaries of domains with distinct magnetic characteristics, and suggests a much larger extension of the syenite-type bodies, which are notably associated with Cu mineralization. A) Analytical signal aeromagnetic map with solid yellow lines delineating positive magnetic anomalies (mostly polygons and few linear anomalies). B) Reduced to pole first vertical derivative filtered data with solid lines corresponding to pronounced linear magnetic anomalies. Color ramp from red (high: 68.0167 nT/m) to blue (low: - 47.8802 nT/m). Image with hill-shading effect. Dotted lines (in A and B) separate domains magnetically 'quiet' from areas of high contrast. C) Compared to the mapped lithologies (see Fig. 1C), the aeromagnetic interpretation indicates that an array of satellite syenite bodies likely extends for > 140 km from NW to SE. MwZ = Mwembeshi Zone.

Fig. 7. Typical breccia types at Kitumba. A) Siderite-cemented syenite breccia. B) Crackle brecciation produced by hematite stockwork veins with late fracture-hosted chalcocite in a quartz porphyry protolith. C) Hematized and potassically altered quartz-porphyry rock in

sharp contact with angular breccia. D) Mosaic breccia with clasts showing transition from early hematite (dark brown in the clasts) to K-alteration in sericitic groundmass. Drillcores S36_1 and S36_33.

Fig. 8. E-W-striking cross-section portraying the schematic interpretation of alteration zoning at Kitumba (modified after Robertson, 2013, and references therein).

Fig. 9. Kitumba prospect lithologies and mineralization: A) Relatively low-altered feldspar porphyritic syenite with a salmon pink, hematite-dusted microcrystalline K-feldspar groundmass. Incipient sericitization of feldspar phenocrysts is apparent (drillcore S1_1). B) Texturally destructive sericite-hematite-carbonate hypogene alteration in syenite breccia. Interstices are filled with hematite-siderite ± quartz ± sulphide (drillcore S36_33). C) Apatite-carbonate-siderite vein. Siderite domains show interstitial pyrite rimmed by chalcopyrite (drillcore KITDD_34). D) Pyrite mineralized clast in hematized syenite breccia (drillcore S36_1, Waller et al., 2014). E) Fracture-filled pyrite and chalcopyrite in altered syenite (drillcore S36_33, Waller et al., 2014). F) Native copper, hematite and calcite in hematite breccia (drillcore S36_15). G) Supergene malachite and chrysocolla mineralization, extending down to 700 m depth (drillcore S36_1). H) Reflected light microphotograph of late, supergene chalcopyrite infilling cracks and partially replacing pyrite mineralization (drillcore S36_33). Ap = apatite; Cal = calcite; Ccp = chalcopyrite; Hem = hematite; Kfs = K-feldspar; Py = pyrite; Sd = siderite.

Fig. 10. Mutoya centre lithologies and mineralization. Mutoya s.s.: A) Magnetite-amphibole-apatite alteration in metasedimentary protolith (drillcore S30_1). B) Massive magnetite replacement partially mineralized with sulphides in disseminations and blebs (pyrite and minor chalcopyrite; drillcore MUM4D). Mushingashi: C) Cm-wide magnetite vein hosting pyrite and (minor) chalcopyrite with late stage mineralized quartz + calcite + siderite. D) Pyrite in orbicular, feathery, disseminated textures in massive magnetite. E) Reflected light microphoto: hypogene magnetite (dark blue) and pyrite crystallization, followed in time by specularite grown as needles (light bluish-gray). F) Reflected light microphoto: thin chalcopyrite rims growing on euhedral pyrite. G) Reflected light microphoto: hematite (light bluish-gray) overprinting magnetite (dark blue). Botryoidal chalcopyrite aggregates (yellow) replaced by late bornite (pink). Mushingashi samples from drillcore MUM6BD. Bn = bornite; Ccp = chalcopyrite; Hem = hematite; Mag = magnetite; Py = pyrite.

Fig. 11. Ranges (light blue bars) and averages (yellow dots) of mass changes (in wt %) for major elements in altered syenites (A) and granites (B) of the analyzed cores, according to

the isocon method. Inferred protoliths: granite Z119A and syenite Z48. Immobile elements during evaluation of mass and chemical changes during alteration: Hf, Ta, Zr (syenite-derived samples); Al_2O_3, Ga, Y (granite-derived samples).

Fig. 12. Chondrite-normalized REE distribution of altered igneous rocks from the Mumbwa cores samples. Inferred precursor patterns (syenite Z48 and granite Z119A) are reported as red dashed lines (chondrite values after Boynton, 1985).

Fig. 13. Alteration boxes and ternary diagrams for analyzed samples displaying chemical mobility and alteration and mineralization vectors (see text). Sample provenance: circle = Kitumba prospect (Sugar Loaf centre); triangle = Mutoya s.s. prospect; square = Mushingashi prospect (Mutoya centre). Red diamonds: inferred protoliths. Alteration: yellow symbols = potassic alteration; grey symbols = sericite-chlorite alteration; green symbols = Ca-alteration. The 4 sericite-chlorite-rich high-Cu mineralized samples from Kitumba are represented as heavy orange contour circles. A) CCPI vs. AI diagram (after Large et al., 2001) discriminating between the main alteration styles; CCPI (chlorite-carbonate-pyrite index) = 100 x [(MgO+FeO)/(MgO+FeO+Na_2O+K_2O)]; AI (Ishikawa alteration index, after Ishikawa et al., 1976) = 100 x [(K_2O+MgO)/(K_2O+MgO+Na_2O+CaO)]. B) AAAI vs. AI diagram showing distinct paths followed by Ca-rich and Ca-poor rocks. AAAI (advanced argillic alteration index, after Wiliams and Davidson, 2004) = 100 x SiO_2/[SiO_2+(10 x MgO)+(10 x CaO)+(10 x Na_2O)]. The boxes in both diagrams represent the inferred field for unaltered rocks (after Wiliams and Davidson, 2004; Bonnet et al., 2005). C) A'FK diagram indicating Fe- or K-gain. A'=Al_2O_3+Fe_2O_3-(K_2O+Na_2O+CaO); F=(FeO+MnO+MgO); K=K_2O; see also Bonnet and Corriveau (2007). D) CKS (C=Ca x 3; S= SiO_2; K=K_2O) diagram showing silicification and Ca-enriched paths, as well as trends for Cu-mineralized rocks.

Prospect	Kitumba											
WGS84 UTM35S	479473 E 8372216 N			479181 E 8374069 N					479235 E 8373891 N			
Sample	**S1_1/0**	**S1_1/1**	**S1_1/2**	**S1_1/4**	**S36_1/4**	**S36_1/5**	**S36_1/8**	**S36_1/12**	**S36_33/6**	**S36_033/7A**	**S36_033/11**	**S36_033/15**
Lithology	syenite	syenite	amph-syenite	metasedim breccia	qz-porphyry granitoid	syenite	metasedim breccia	metasedim breccia	qz-porphyry granitoid	qz-porphyry granitoid	metasedimentary rock	metasedimentary rock
Depth (m)	15.25-15.62	19.90-20.12	95.84-96.14	253.72-254.11	220.55-220.96	307.88-308.11	347.68-347.88	436.16-436.56	106.06-106.30	113.02-113.27	173.83-174.10	426.05-426.25
Main alteration	hem+potassic	hem+potassic	hem+potassic	hem+potassic (± chlorite)	potassic	hem+potassic	hem+potassic (± chlorite)	hem+potassic (± chlorite)	hem+potassic	hem (± potassic)	hem+potassic (± chlorite)	hem+potassic (± chlorite)
Sulphide mineralized	no	no	no	no	no	weakly	weakly	weakly	no	no	highly	highly
SiO_2	59.68	55.11	60.67	48.75	82.13	54.36	51.30	50.33	78.13	59.33	51.06	34.08
TiO_2	1.32	1.16	1.18	1.04	0.14	0.97	1.08	0.86	0.19	0.31	1.20	0.68
Al_2O_3	18.89	16.53	17.00	13.72	9.14	15.31	15.36	13.61	10.48	8.23	14.62	10.57
FeOtot	5.57	11.91	5.40	18.86	1.07	7.03	12.82	15.81	2.01	20.60	13.58	30.90
MnO	0.09	0.15	0.41	1.89	0.02	0.89	1.63	1.96	0.30	0.04	1.48	2.01
MgO	0.28	0.32	0.51	1.28	0.10	0.52	0.89	1.34	0.12	0.11	0.91	1.20
CaO	0.07	0.08	0.69	0.84	0.05	0.77	1.00	0.90	0.05	0.07	1.12	0.98
Na_2O	0.03	0.01	0.04	0.01	0.02	0.06	0.01	0.02	0.01	0.06	0.00	0.14
K_2O	12.27	10.82	12.14	7.19	6.61	11.51	10.91	9.62	7.20	4.59	11.01	6.35
P_2O_5	0.26	0.43	0.46	0.50	0.05	0.43	0.63	0.49	0.22	0.23	0.71	0.56
LOI	2.10	2.53	4.24	12.64	0.85	6.04	9.59	11.55	1.28	1.75	9.83	18.21
total	100.57	99.05	102.74	106.73	100.18	97.88	105.21	106.49	100.00	95.32	105.53	105.68
Ba	2974	3106	1277	652	2363	1869	1053	2686	2832	351	3366	717
Co	31.05	47.08	16.17	50.81	3.94	111.33	269.26	151.47	26.08	6.84	97.94	635.79
Cr	11.29	9.74	14.35	40.94	10.36	16.74	9.75	9.68	10.19	17.13	34.13	13.78
Cs	0.61	0.61	2.08	1.27	0.53	0.83	1.20	0.87	0.47	0.67	1.05	0.55
Cu	85.18	169.99	10.50	104.35	1512.60	307.08	2667.08	76.70	527.57	658.53	43.43	11630.84
Ga	21.97	21.41	21.64	19.65	11.91	19.43	19.85	18.31	16.09	12.19	16.83	15.89
Hf	9.96	8.22	8.03	6.55	5.33	8.07	8.68	7.91	7.19	7.45	4.71	3.90
Mo	3.17	3.48	2.58	69.58	4.49	3.55	7.97	7.25	8.56	55.20	12.89	2.71
Nb	57.46	52.11	27.61	30.28	14.43	26.95	51.19	43.71	25.68	35.74	21.31	14.49
Ni	16.12	23.05	15.24	44.24	13.34	29.59	54.66	41.97	14.36	19.69	66.92	363.68
Pb	7.10	8.37	4.80	3.64	3.50	5.90	10.38	4.35	2.47	15.66	4.55	8.90
Rb	214.95	186.11	224.40	177.65	145.68	239.43	264.61	223.51	145.92	85.13	253.63	169.32
Sc	13.44	12.76	12.34	14.49	8.65	17.17	7.89	7.32	7.37	3.97	17.75	7.26
Sr	278.57	281.08	219.94	85.30	58.20	231.78	159.89	199.61	63.07	60.01	284.41	140.45
Ta	2.33	2.08	1.66	1.67	1.13	1.52	2.21	2.57	1.75	1.28	0.97	0.79
Th	48.58	37.24	42.40	37.79	18.86	41.95	38.75	34.50	24.28	49.60	24.30	21.45
U	13.79	14.21	10.54	49.38	15.54	18.96	25.03	18.44	22.13	82.11	21.42	8.94
V	174.19	236.89	126.62	165.02	73.52	84.84	103.03	103.50	37.24	164.55	124.00	147.57
Y	63.03	40.64	34.38	48.61	27.17	31.46	55.35	42.40	65.86	41.90	49.98	29.41
Zn	23.67	36.40	31.46	87.24	30.62	37.83	205.76	95.18	31.50	34.39	94.04	59.01
Zr	391.12	329.93	326.72	263.98	191.30	318.84	346.20	321.03	235.86	246.26	169.92	156.69
La	164.79	101.51	103.70	638.51	154.97	85.13	142.78	103.86	116.99	924.68	171.93	85.15
Ce	338.50	236.17	236.70	911.15	231.90	180.61	283.79	190.50	170.92	1085.95	332.15	156.57
Pr	37.63	27.55	26.67	83.26	18.63	20.82	30.21	20.57	15.37	76.49	34.31	16.22
Nd	132.51	97.84	94.34	250.39	53.62	77.15	102.62	72.93	48.52	185.44	114.85	56.12
Sm	20.34	14.64	14.29	29.75	7.31	12.09	15.28	11.54	7.09	17.48	16.56	9.03
Eu	4.96	4.18	3.25	7.28	2.21	2.95	3.86	3.28	1.80	4.94	4.66	2.69
Gd	15.12	10.29	10.04	19.34	6.00	9.59	12.72	8.35	7.75	11.58	13.83	7.15
Tb	2.10	1.32	1.22	2.16	0.79	1.16	1.80	1.34	1.53	1.53	1.79	0.95
Dy	12.26	7.20	6.79	10.60	4.39	6.32	10.58	8.02	11.30	8.45	10.21	5.56
Ho	2.45	1.45	1.30	1.89	0.97	1.24	2.02	1.62	2.47	1.58	2.00	1.11
Er	6.66	4.11	3.48	5.02	2.72	3.56	5.54	4.61	7.59	4.16	5.26	3.03
Tm	0.93	0.60	0.48	0.71	0.39	0.52	0.74	0.62	1.08	0.56	0.67	0.45
Yb	6.00	4.01	3.32	4.73	2.42	3.45	4.75	4.12	7.27	3.54	4.66	2.93
Lu	0.85	0.62	0.50	0.70	0.37	0.51	0.66	0.62	0.99	0.48	0.69	0.44

Prospect	Mutoya *s.s.*				Mushingashi							
WGS84 UTM35S	475748 E 8376545 N				474753 E 8380393 N						INFERRED PROTOLITHS	
Sample	**MUM4D/6**	**MUM4D/7**	**MUM4D/8**	**MUM4D/10**	**MUM6BD/1**	**MUM6BD/2**	**MUM6BD/3**	**MUM6BD/4**	**MUM6BD/5**	**MUM6BD/6**	**Z48**	**Z119A**
Lithology	?	syenite	?	magmatic breccia	syenite breccia?	syenite?	syenite breccia?	syenite?	syenite breccia?	syenite?	syenite	granite
Depth (m)	545.85-545.71	605.87-606.32	813.71-813.90	836.19-836.52	499.37-499.71	507.61-507.86	514.35-514.70	529.41-529.65	582.39-582.78	606.22-606.61		
Main alteration	mt+chlorite +epidote	hem+potassic	mt+chlorite +epidote	mt+potassic+ chlorite+carbonate	mt+potassic+ chlorite+epidote	mt+potassic+ chlorite+epidote	mt+potassic+ chlorite+epidote	mt+potassic+ chlorite	mt+potassic+ chlorite+epidote	mt+potassic+ chlorite+epidote		
Suphide mineralized	highly	weakly	weakly	no	weakly	weakly	weakly	weakly	weakly	weakly	no	no
SiO_2	24.89	55.78	35.98	53.88	42.82	41.17	33.29	49.69	42.76	46.56	64.70	70.21
TiO_2	0.22	0.55	0.31	0.51	1.13	1.28	0.44	1.10	0.96	0.93	0.51	0.48
Al_2O_3	0.85	16.45	14.59	13.15	15.87	16.79	11.06	17.76	14.04	14.97	17.91	14.30
FeOtot	40.83	7.65	10.38	5.73	8.76	17.11	16.15	12.21	10.47	8.44	2.32	3.45
MnO	0.64	0.90	0.35	0.23	0.42	0.41	0.46	0.27	0.39	0.36	0.02	0.09
MgO	7.60	0.81	3.89	2.47	3.03	5.44	2.57	3.81	2.21	2.00	0.95	0.56
CaO	7.54	2.48	22.35	7.63	9.06	4.16	14.61	1.68	12.43	11.44	2.47	2.04
Na_2O	0.03	0.20	0.06	0.12	0.11	0.00	0.00	0.06	0.04	0.48	4.26	2.45
K_2O	0.07	11.86	0.46	8.80	7.62	5.97	5.45	8.95	6.39	7.72	6.66	5.33
P_2O_5	0.03	0.21	0.36	0.18	0.24	0.41	0.41	0.42	0.31	0.25	0.17	0.12
LOI	0.63	4.66	5.52	4.01	6.33	7.72	8.24	4.51	4.16	3.53	0.25	0.31
total	83.34	101.55	94.24	96.71	95.41	100.46	92.68	100.46	94.18	96.68	100.22	99.34
Ba	18	1986	77	2835	746	453	732	1078	2258	969	1167.77	1085.23
Co	175.25	25.07	60.30	56.28	80.99	110.62	67.39	67.90	78.27	42.27	5.24	5.54
Cr	10.84	14.26	21.94	11.43	18.54	31.45	16.46	20.55	39.11	27.39	14.99	12.54
Cs	0.06	3.47	0.11	0.74	2.75	12.53	3.22	9.65	1.98	2.16	3.10	3.00
Cu	2184.05	18.03	836.64	218.44	712.96	1064.10	887.63	673.69	219.73	825.91	14.72	13.02
Ga	10.35	23.90	43.28	16.24	21.66	19.98	17.58	19.22	15.32	14.23	20.02	22.4
Hf	0.27	12.52	5.95	8.87	7.79	8.54	5.72	8.16	7.11	7.35	7.99	13.86
Mo	1.13	1.37	1.09	1.13	2.04	2.17	2.38	2.47	2.06	1.96	0.62	0.77
Nb	0.38	76.07	15.95	40.90	27.09	32.50	21.79	28.02	24.36	33.90	26.15	22.46
Ni	123.29	15.19	32.29	29.12	40.85	23.58	41.85	15.42	21.65	49.19	10.81	10.40
Pb	34.59	10.58	7.35	6.14	21.51	17.76	6.19	13.29	4.51	12.82	6.36	16.86
Rb	1.38	288.32	10.66	206.51	376.91	394.37	181.52	382.75	241.89	224.45	135.68	180.52
Sc	7.74	6.35	13.01	16.31	15.16	15.39	11.20	12.31	16.08	16.09	9.08	16.20
Sr	24.91	194.31	2070.12	326.68	258.13	108.41	280.50	171.27	322.85	482.21	552.48	174.14
Ta	0.09	3.11	1.09	2.21	1.67	1.66	1.23	1.64	2.08	2.02	1.60	1.10
Th	1.68	45.92	12.56	36.28	28.81	27.70	18.99	40.72	46.90	31.93	40.69	21.07
U	1.31	11.64	12.75	9.57	17.14	17.90	14.71	24.04	22.84	20.88	3.97	4.17
V	163.63	173.52	131.06	40.21	102.26	127.89	109.67	114.88	130.36	109.51	60.44	28.59
Y	2.76	41.74	17.45	24.33	61.74	64.00	25.24	48.54	57.74	93.33	31.48	54.86
Zn	296.97	29.52	62.77	53.76	148.64	141.38	109.84	183.21	69.23	107.13	15.26	67.05
Zr	7.58	509.39	240.85	384.51	306.46	323.99	231.45	327.43	244.66	301.61	311.02	539.60
La	13.83	42.26	399.81	46.25	126.53	114.06	89.62	83.89	148.68	95.15	151.86	66.71
Ce	29.54	96.96	450.34	115.46	268.62	220.73	180.69	189.41	277.45	178.14	264.58	136.63
Pr	2.85	11.43	33.74	13.70	27.10	23.05	18.94	17.93	26.10	17.00	27.05	16.15
Nd	7.95	43.00	79.83	47.29	85.08	81.13	60.09	49.86	75.21	53.38	92.19	63.74
Sm	0.91	7.80	6.67	6.65	12.86	14.61	8.45	6.31	10.68	9.43	13.41	13.13
Eu	0.21	1.89	4.80	2.12	4.82	4.30	2.37	3.09	4.90	3.27	2.66	2.80
Gd	1.03	6.82	7.57	5.89	15.76	14.01	6.84	7.29	14.17	13.23	8.65	11.80
Tb	0.13	1.04	0.60	0.82	2.11	2.09	0.85	1.25	1.84	2.13	1.12	1.73
Dy	0.55	6.88	2.86	4.37	12.66	12.87	4.94	8.30	10.99	14.85	6.33	10.61
Ho	0.11	1.48	0.62	0.86	2.58	2.70	0.97	1.91	2.28	3.38	1.18	2.05
Er	0.28	4.81	1.83	2.58	7.50	8.46	2.71	6.15	6.53	10.84	3.23	5.89
Tm	0.03	0.83	0.25	0.36	1.13	1.26	0.42	0.96	0.97	1.68	0.47	0.80
Yb	0.26	6.39	1.62	2.71	7.46	9.04	3.01	6.79	6.77	12.12	3.20	5.11
Lu	0.06	0.96	0.26	0.41	1.09	1.35	0.45	1.10	1.02	2.05	0.47	0.76

Table 1. Chemical composition and alteration/mineralization features of the Mumbwa cores (major elements in wt%, trace elements in ppm). Chemistry of inferred protoliths Z48 (syenite) and Z119A (granite) are included.

Sample no.	WGS84 UTM35S	Center/prospect	Analyzed min.	$\delta^{34}S$	Depth (m)	Origin	Host rock	Alteration	Sulfide assemblage
		SUGAR LOAF							
S36_1/10	479181 E 8374069 N	Kitumba	Ccp	4.3	377	hypogene	syenite	potassic, carbonate	Py+Ccp
S36_1 new		Kitumba	Py	5.5	664	hypogene	syenite breccia	hematite	Py+Ccp
S36_33/13-14	479235 E 8373891 N	Kitumba	Py+Ccp	4.4	422	hypogene	syenite	potassic, carbonate	Py+Ccp
KITDD_27/1	479092 E 8673885 N	Kitumba	Cc+Ccp	6.6	232	supergene	syenite	hematite	Cc+Ccp
KITDD_27/2		Kitumba	Cc+Ccp	7.1	244	supergene	syenite	kaolinite	Cc+Ccp
KITDD_27/3		Kitumba	Py+Cc	6.3	303	supergene	syenite	potassic	Py+Cc+Mal+Cu
KITDD_27/4		Kitumba	Py+Cc	7.0	312	supergene	syenite	kaolinite, sericite	Py+Cc
KITDD_27/5		Kitumba	Py+Cc	7.0	313	supergene	syenite	hematite	Py+Cc
KITDD_27/6		Kitumba	Py+Ccp	6.4	326	transitional	syenite	kaolinite, sericite	Py+Ccp
KITDD_27/7		Kitumba	Ccp	6.5	358	transit-hypog	syenite	potassic, hematite	Ccp
KITDD_27/8		Kitumba	Ccp	6.8	361	hypogene	syenite	carbonate, siderite	Ccp
KITDD_27/9		Kitumba	Ccp	7.1	365	hypogene	syenite	potassic	Ccp
KITDD_27/10		Kitumba	Ccp	7.0	387	hypogene	syenite	potassic,carbonate	Ccp
KITDD_27/11		Kitumba	Py+Ccp	6.4	432	hypogene	syenite	potassic	Py+Ccp
KITDD_27/12		Kitumba	Py+Ccp	7.3	489	hypogene	porphyritic granite	sericite	Py+Ccp
KITDD_27/13		Kitumba	Py+Ccp	7.1	510	hypogene	syenite	potassic, sericite	Py+Ccp
KITDD_34/1	479032 E 8374195 N	Kitumba	Py	7.6	624	hypogene	syenite	potassic, sericite	Py
KITDD_34/2		Kitumba	Py	7.4	628	hypogene	syenite	potassic, sericite	Py
		MUTOYA							
MUM4D/4	475748 E 8376545 N	Mutoya s.s.	Py	1.4	102	supergene	metasedim. breccia	carbonate, silica	Py
MUM4D/6		Mutoya s.s.	Py+Ccp	3.8	545	hypogene	?	magnetite, chlorite, epidote, carbonate	Py+Ccp
MUM4D/9		Mutoya s.s.	Py	4.2	832	hypogene	metasedim. breccia	epidote, chlorite, magnetite, biotite	Py
MUM6BD/1	474753 E 8380393 N	Mushingashi	Py	4.4	499	hypogene	syenite breccia?	magnetite, potassic, chlorite, epidote	Py + Cpy (trace)
MUM6BD/3		Mushingashi	Py	3.7	514	hypogene	syenite breccia?	magnetite, potassic, chlorite, epidote	Py + Cpy (trace)
MUM6BD/5		Mushingashi	Py	4.2	582	hypogene	syenite breccia?	magnetite, potassic, chlorite, epidote	Py + Cpy (trace)
MUM6BD/7		Mushingashi	Py	3.5	812	hypogene	mt replacement	magnetite	Py+Ccp
MUM6/BD8		Mushingashi	Py	3.5	852	hypogene	mt replacement	magnetite, carbonate	Py
Z 77	442792 E 8347268 N	Hook batholith	Py	8.6	surface	magmatic	quartz-monzonite	-	Py

Table 2. Sulphur isotope values for sulphide minerals from the Mumbwa district. Cc=chalcocite; Ccp=chalcopyrite; Cu=native copper; Mal=malachite; Py=pyrite.

ALTERATION TYPE	PRIMARY-HYDROTHERMAL HYPOGENE	SECONDARY SUPERGENE
MAGNETITE		
POTASSIC		
CARBONATE (ANKERITE)		
CARBONATE (SIDERITE-ANKERITE)		
HEMATITE		
SERICITE		
ARGILLIC		
APATITE-FE-CARBONATE-HEMATITE		
GOETHITE-LIMONITE		

Table 3. Schematic representation of the temporal sequence of alteration phases at Kitumba. Note that coeval alterations do not always imply spatial association (e.g., carbonate-ankerite never occurs in hematite- and kaolinite-rich zones).

Immobile elements: Al_2O_3, Gd, Y

		Slope obtained by linear regr.:	0.5877		Slope obtained by linear regr.:	0.8355		Slope obtained by linear regr.:	0.6123	
Sample	precursor rock **granite Z119A** Co	qz-porph granite **S36_1/4** CA	Slope data point CA/Co	Gain/loss in wt% mass relative to Co	qz-porph granite **S36_33/6** CA	Slope data point CA/Co	Gain/loss in wt% mass relative to Co	qz-porph granite **S36_33/7A** CA	Slope data point CA/Co	Gain/loss in wt% mass relative to Co
SiO_2	70.21	82.13	1.17	0.99	78.13	1.11	0.33	59.33	0.85	0.38
TiO_2	0.48	0.14	0.29	-0.50	0.19	0.40	-0.53	0.31	0.65	0.05
Al_2O_3	14.30	9.14	0.64	0.09	10.48	0.73	-0.12	8.23	0.58	-0.06
FeOtot	4.44	1.37	0.31	-0.47	2.59	0.58	-0.30	26.50	5.97	8.75
MnO	0.09	0.02	0.22	-0.62	0.30	3.33	2.99	0.04	0.44	-0.27
MgO	0.56	0.10	0.18	-0.70	0.12	0.21	-0.74	0.11	0.20	-0.68
CaO	2.04	0.05	0.03	-0.96	0.05	0.03	-0.97	0.07	0.03	-0.94
Na_2O	2.45	0.02	0.01	-0.99	0.01	0.00	-1.00	0.06	0.02	-0.96
K_2O	5.33	6.61	1.24	1.11	7.20	1.35	0.62	4.59	0.86	0.41
P_2O_5	0.12	0.05	0.42	-0.29	0.22	1.83	1.19	0.23	1.92	2.13

Immobile elements: Hf, Zr, Ta

		Slope obtained by linear regr.:	1.2608		Slope obtained by linear regr.:	1.0618		Slope obtained by linear regr.:	1.0429		Slope obtained by linear regr.:	1.0209		Slope obtained by linear regr.:	1.6343	
Sample	precursor rock **syenite Z48** Co	syenite **S1_1/0** CA	Slope data point CA/Co	Gain/loss in wt% mass relative to Co	syenite **S1_1/1** CA	Slope data point CA/Co	Gain/loss in wt% mass relative to Co	syenite **S1_1/2** CA	Slope data point CA/Co	Gain/loss in wt% mass relative to Co	syenite **S36_1/5** CA	Slope data point CA/Co	Gain/loss in wt% mass relative to Co	syenite **MUM4D/7** CA	Slope data point CA/Co	Gain/loss in wt% mass relative to Co
SiO_2	64.70	59.68	0.92	-0.27	55.11	0.85	-0.20	60.67	0.94	-0.10	54.36	0.84	-0.18	55.78	0.86	-0.47
TiO_2	0.51	1.32	2.59	1.05	1.16	2.28	1.14	1.18	2.31	1.22	0.97	1.90	0.86	0.55	1.08	-0.34
Al_2O_3	17.91	18.89	1.06	-0.16	16.53	0.92	-0.13	17.00	0.95	-0.09	15.31	0.86	-0.16	16.45	0.92	-0.44
FeOtot	2.99	7.17	2.40	0.90	15.32	5.13	3.83	6.95	2.33	1.23	9.05	3.03	1.97	9.84	3.30	1.03
MnO	0.02	0.09	4.50	2.57	0.15	7.50	6.06	0.41	20.50	18.66	0.89	44.50	42.59	0.90	45.00	26.67
MgO	0.95	0.28	0.30	-0.77	0.32	0.34	-0.68	0.51	0.54	-0.49	0.52	0.55	-0.46	0.81	0.85	-0.48
CaO	2.47	0.07	0.03	-0.98	0.08	0.03	-0.97	0.69	0.28	-0.73	0.77	0.31	-0.69	2.48	1.00	-0.38
Na_2O	4.26	0.03	0.01	-0.99	0.01	0.00	-1.00	0.04	0.01	-0.99	0.06	0.01	-0.99	0.20	0.05	-0.97
K_2O	6.66	12.27	1.84	0.46	10.82	1.63	0.53	12.14	1.82	0.75	11.51	1.73	0.69	11.86	1.78	0.10
P_2O_5	0.17	0.26	1.53	0.21	0.43	2.53	1.38	0.46	2.71	1.59	0.43	2.53	1.48	0.21	1.24	-0.24

2-COLUMN FITTING IMAGE

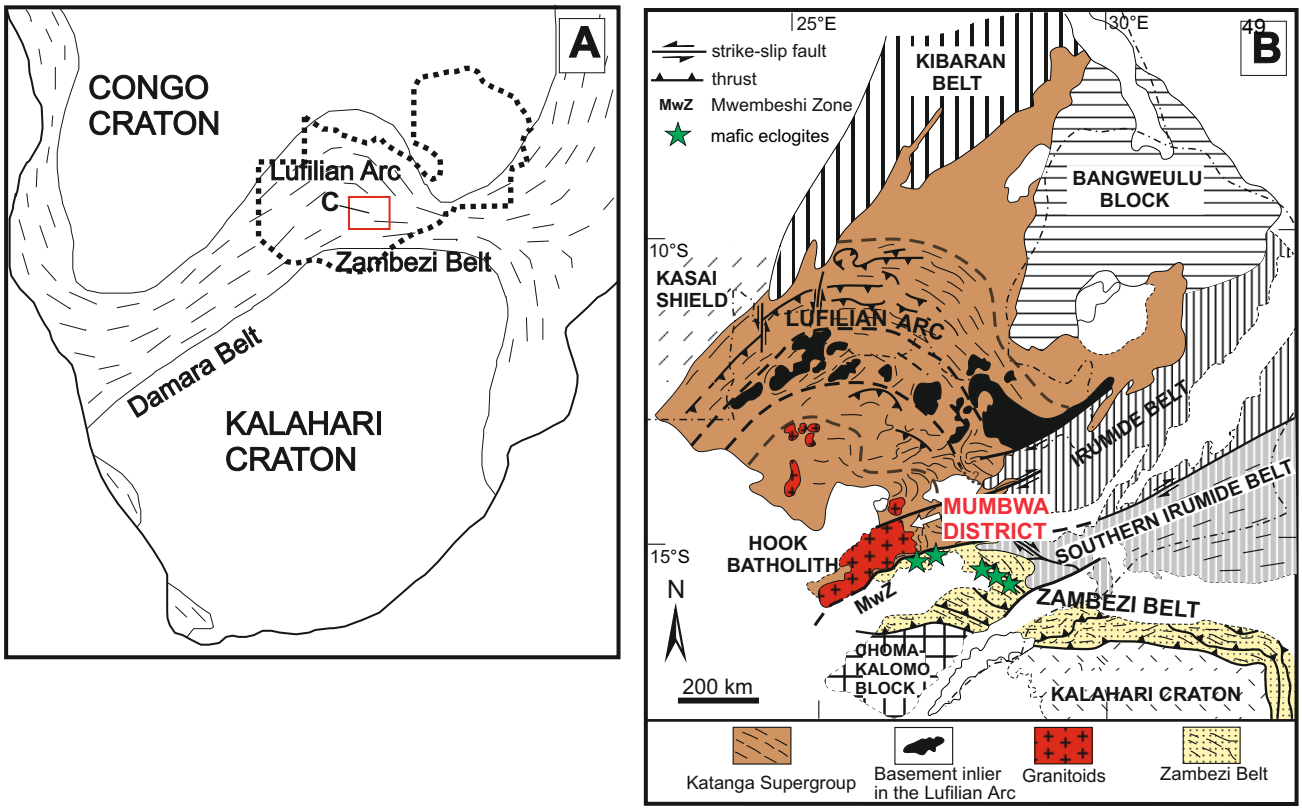

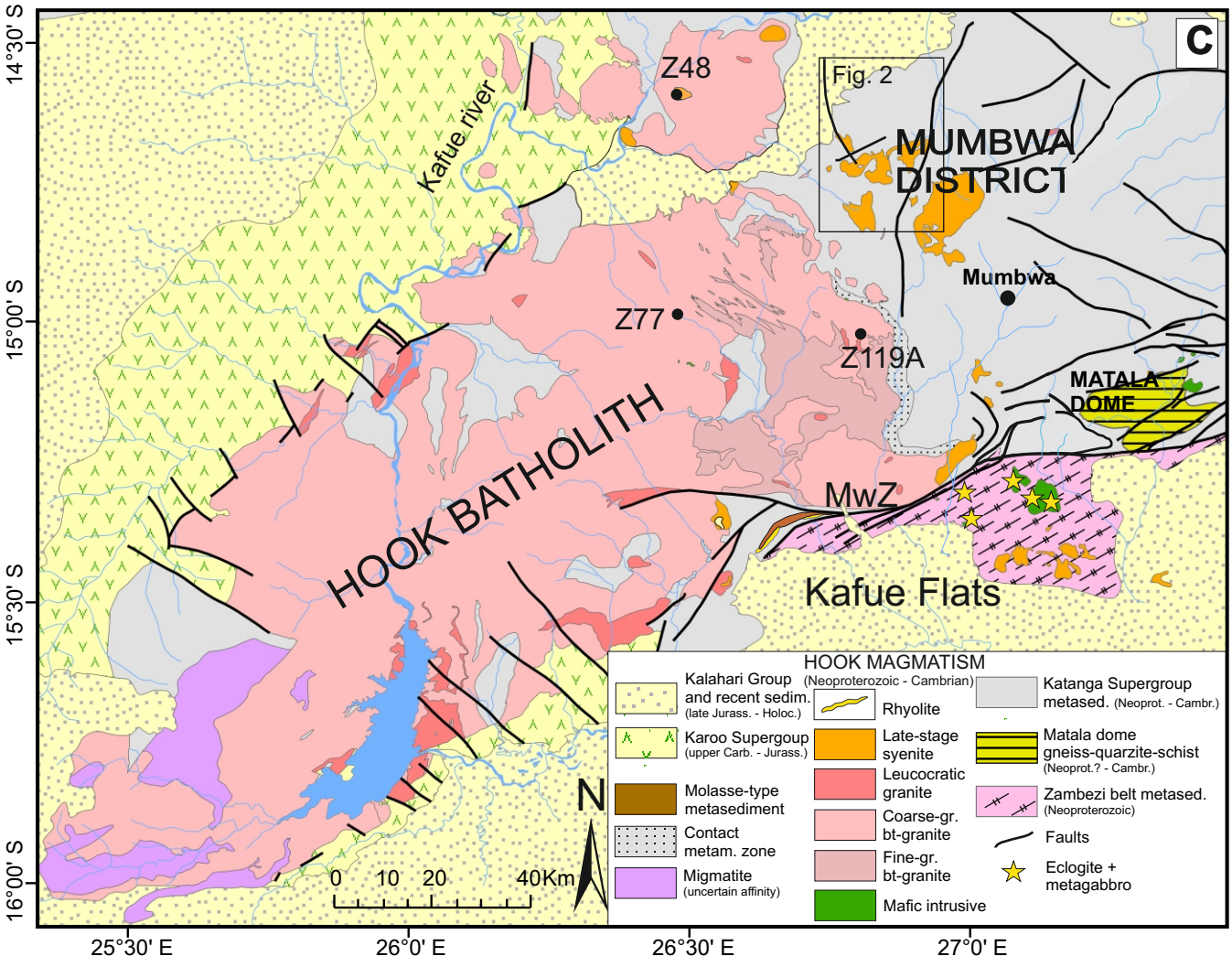

Fig. 1. Regional and local geological setting. A) Relationship between the Congo and Kalahari cratons and the main Pan-African mobile belts. B) Geological map of the Lufilian and Zambezi belts (modified after John et al., 2004a; Porada, 1989; Selley et al., 2005). C) Simplified geological map of the Hook batholith area (modified after Naydenov et al., 2014 and Milani et al., 2015). Sample location of Quartz-monzonite Z77 and inferred protoliths (Z48 - syenite, Z119A - granite) is shown; MwZ = Mwembeshi Zone.

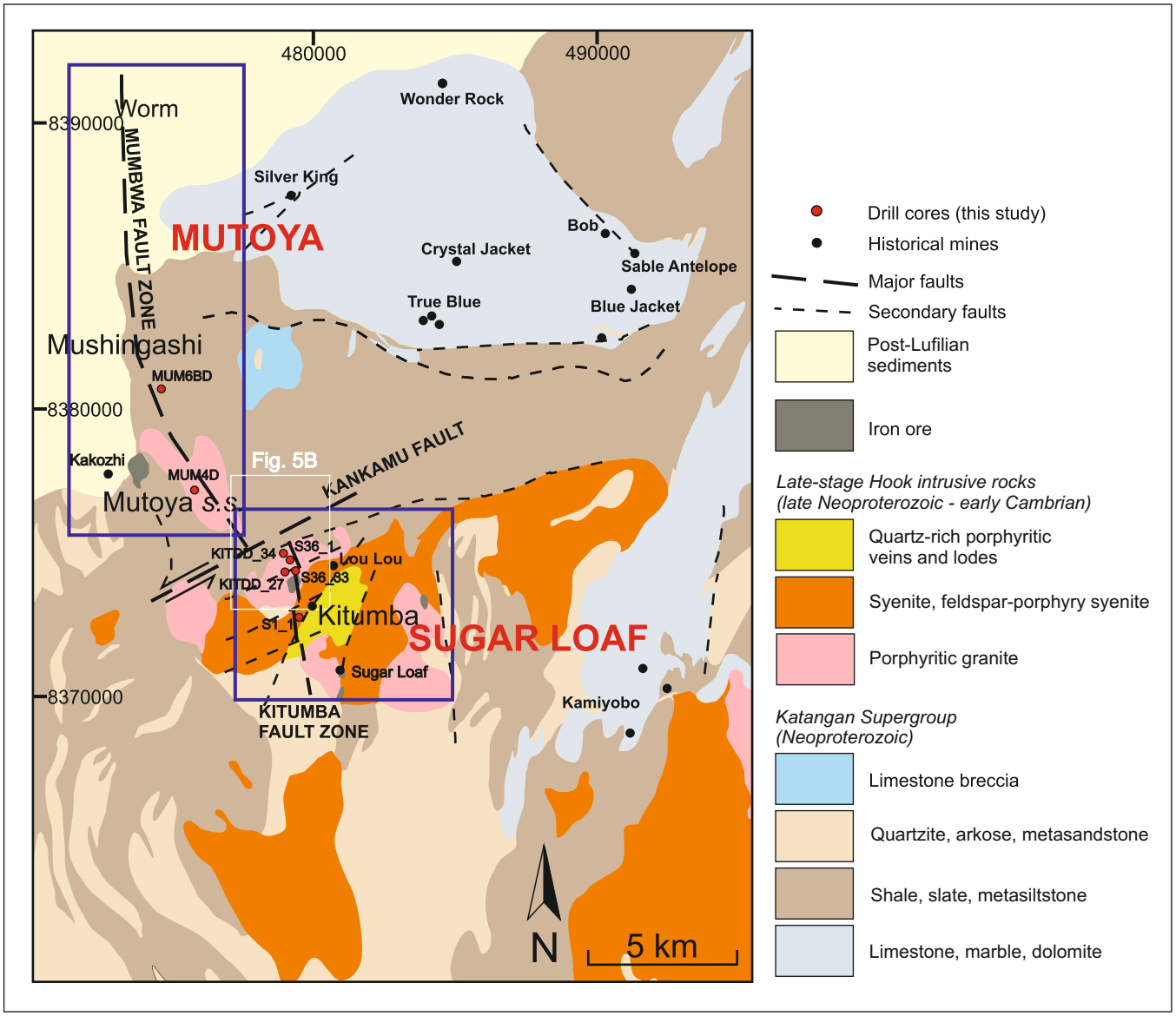

Fig. 2. Geological map of the Mumbwa district (modified from the 1:100,000 scale geological map of Zambia - degree sheet 1426, SE quarter, Cikin and Drysdall, 1971), with historical base-metal occurrences, main tectonic lineaments and location of studied drillcores. Boxes outline the Sugar Loaf and Mutoya mineralized centres.

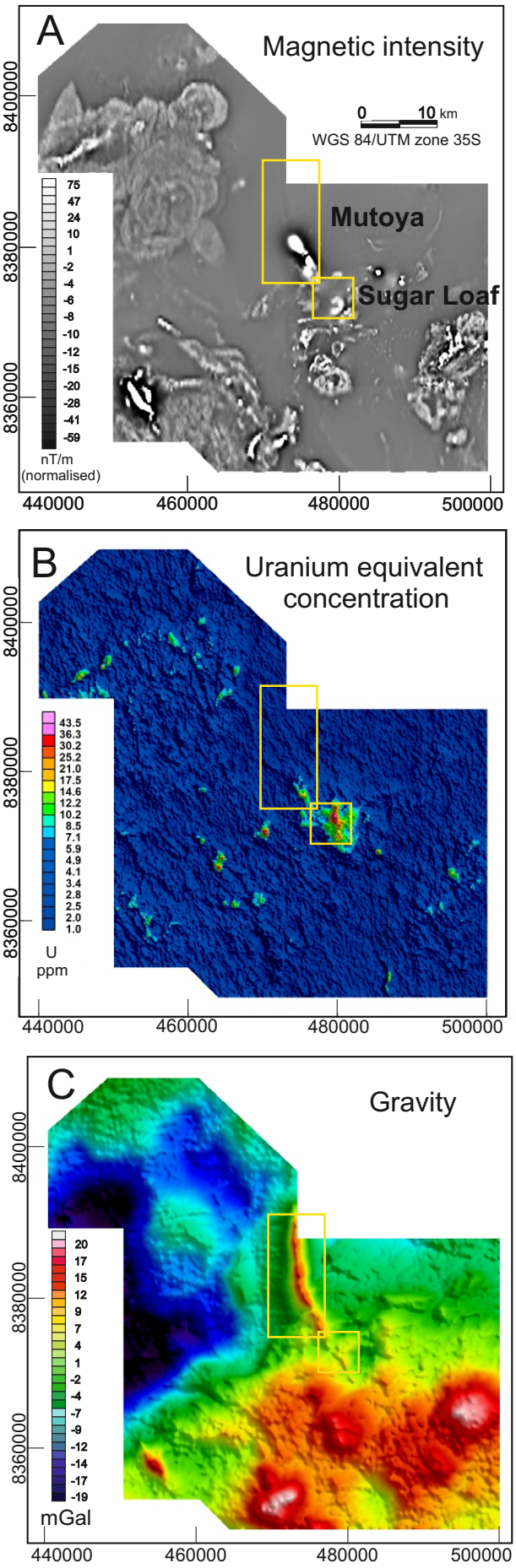

Fig. 3. Representative data from the aerial Falcon survey over the Mumbwa area at 400 m line spacing. A) Tota Magnetic Intensity – Reduced to the Pole (TMI RTP) with First Vertical Derivative (1VD) and Automatic Gain Control (AGC) filter. B) Uranium equivalent concentration. C) Airborne gravity gradient (AGG) Bouguer gravity terrain corrected at 2.67 g/cm^3.

SINGLE-COLUMN IMAGE

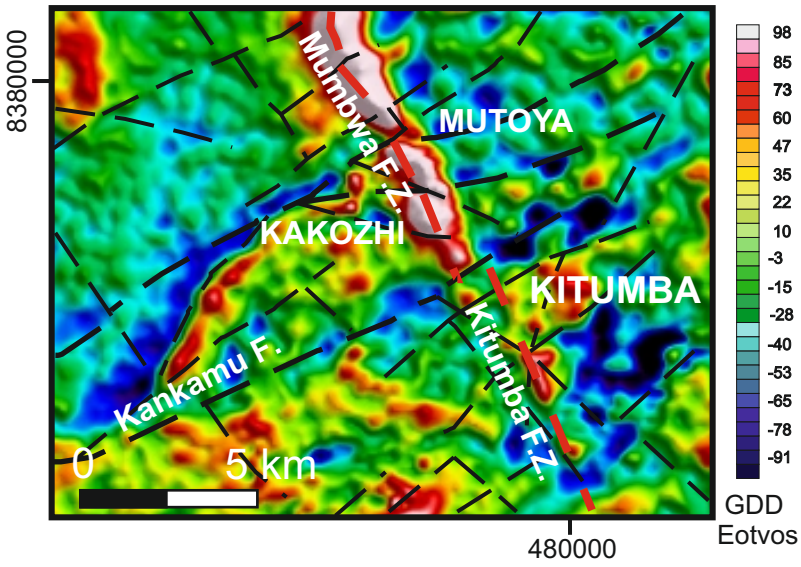

Fig. 4. Vertical gravity gradient (GDD) terrain corrected at 2.67 g/cm^3 over the Kitumba, southern Mutoya and Kakozhi prospects. The inferred lineaments are according to B Billiton structural interpretation.

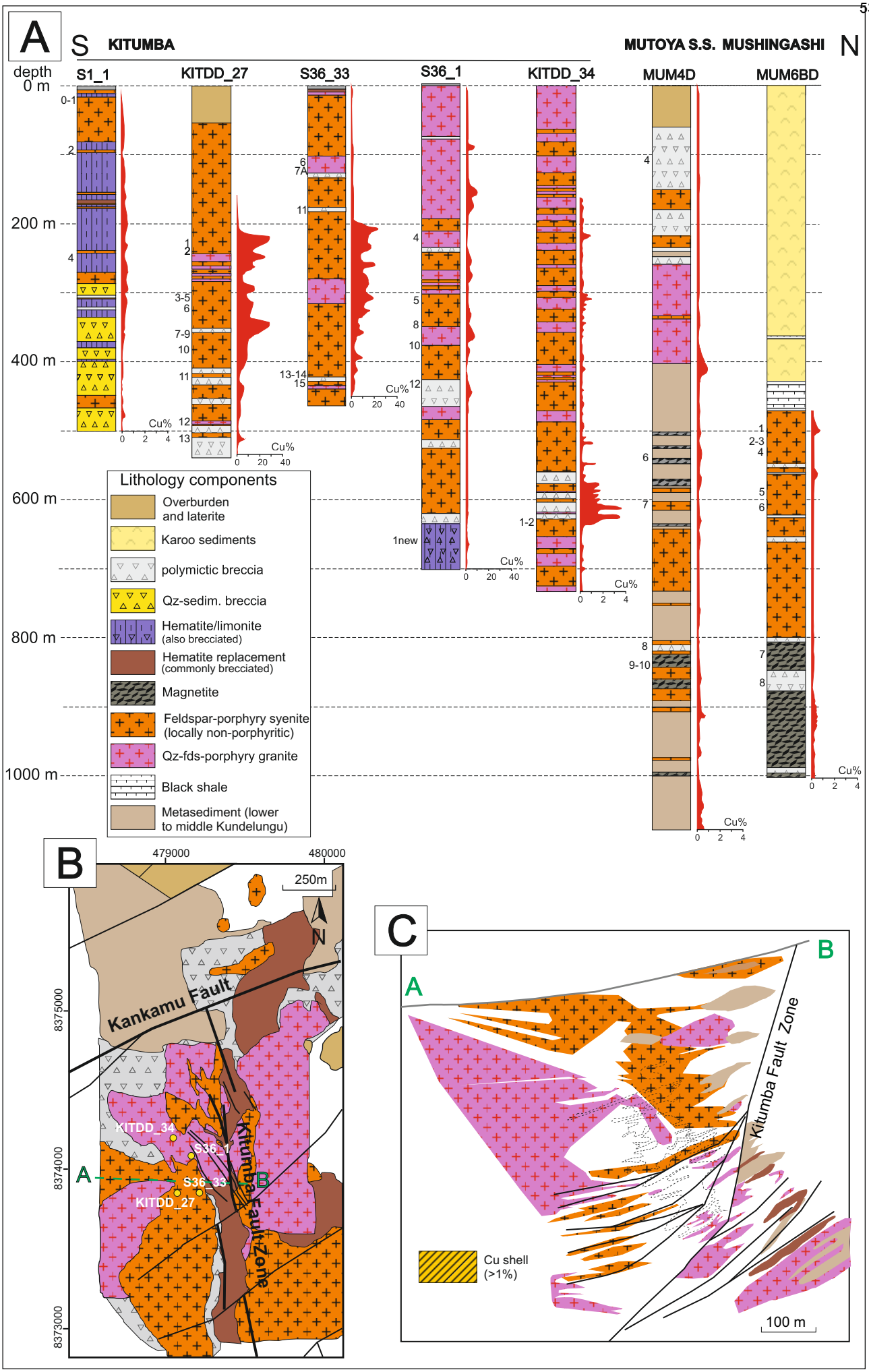

Fig. 5. A) Lithological borehole logs from the studied drillcores from Kitumba and Mutoya (Mutoya s.s. and Mushingashi, courtesy of MSA group). Locations of all boreholes are shown in Fig. 2. Numbers to the left of the columns refer to labels of samples analyzed for element geochemistry and/or sulphur isotopes. Copper contents (in wt%) are also reported (maximum scales at 4 or 40 % Cu). B) Geological map of the Kitumba prospect with major lineaments and drill cores location (S1_1 out of map; modified after Waller et al., 2014). C) Interpretative geological section at Kitumba, drawn at ca. 8.373,900 mN, azimuth 183 on the basis of surface mapping and drill core interpolation (see also B) for location).

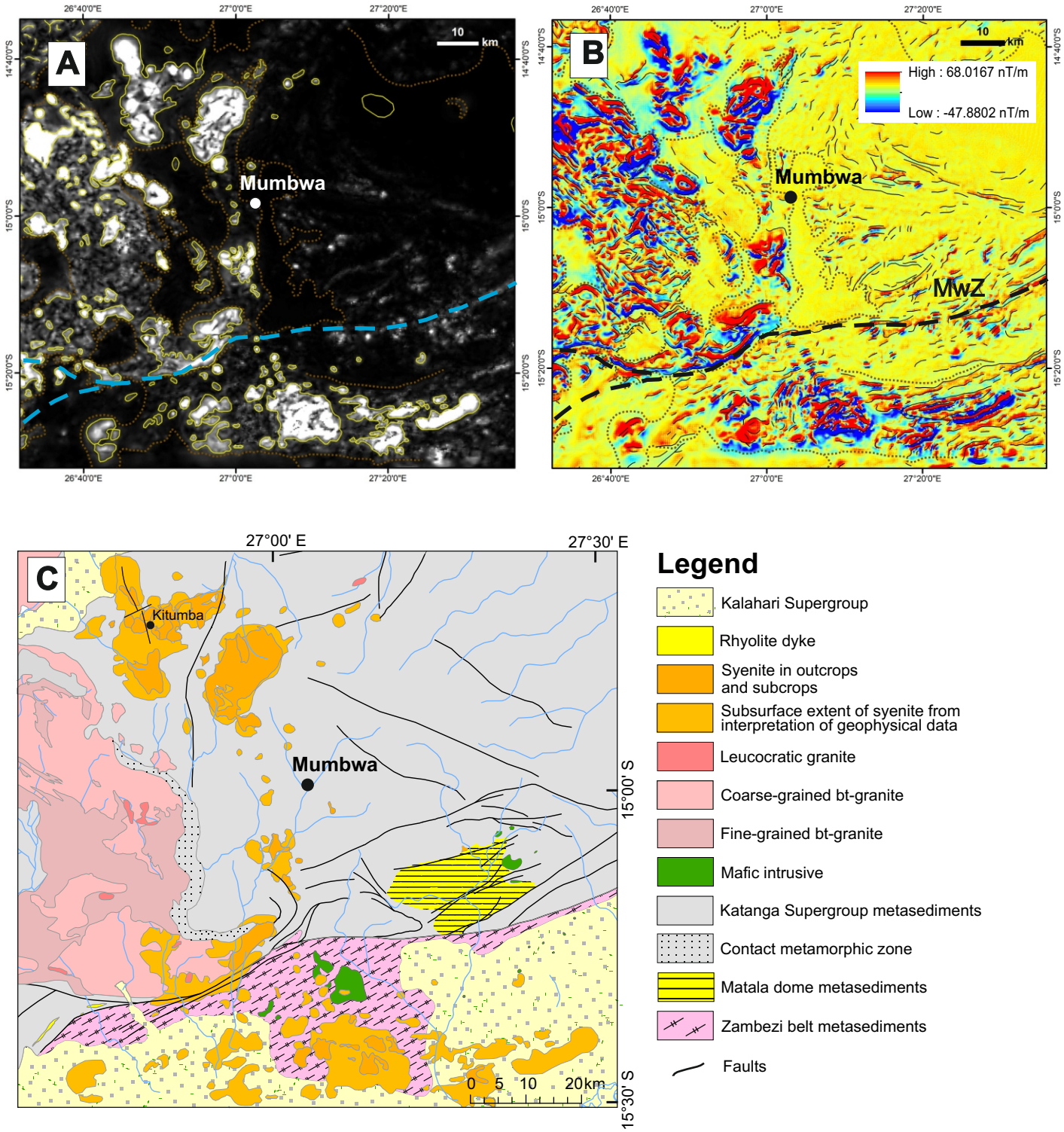

Fig. 6. Line drawing applied to the regional airborne geophysical survey defines boundaries of domains with distinct magnetic characteristics, and suggests a much larger extension of the syenite-type bodies, which are notably associated with Cu mineralization. A) Analytical signal aeromagnetic map with solid yellow lines delineating positive magnetic anomalies (mostly polygons and few linear anomalies). B) Reduced to pole first vertical derivative filtered data with solid lines corresponding to pronounced linear magnetic anomalies. Color ramp from red (high: 68.0167 nT/m) to blue (low: - 47.8802 nT/m). Image with hill-shading effect. Dotted lines (in A and B) separate domains magnetically 'quiet' from areas of high contrast. C) Compared to the mapped lithologies (see Fig. 1C), the aeromagnetic interpretation indicates that an array of satellite syenite bodies likely extends for > 140 km from NW to SE. MwZ = Mwembeshi Zone.

2-COLUMN FITTING IMAGE

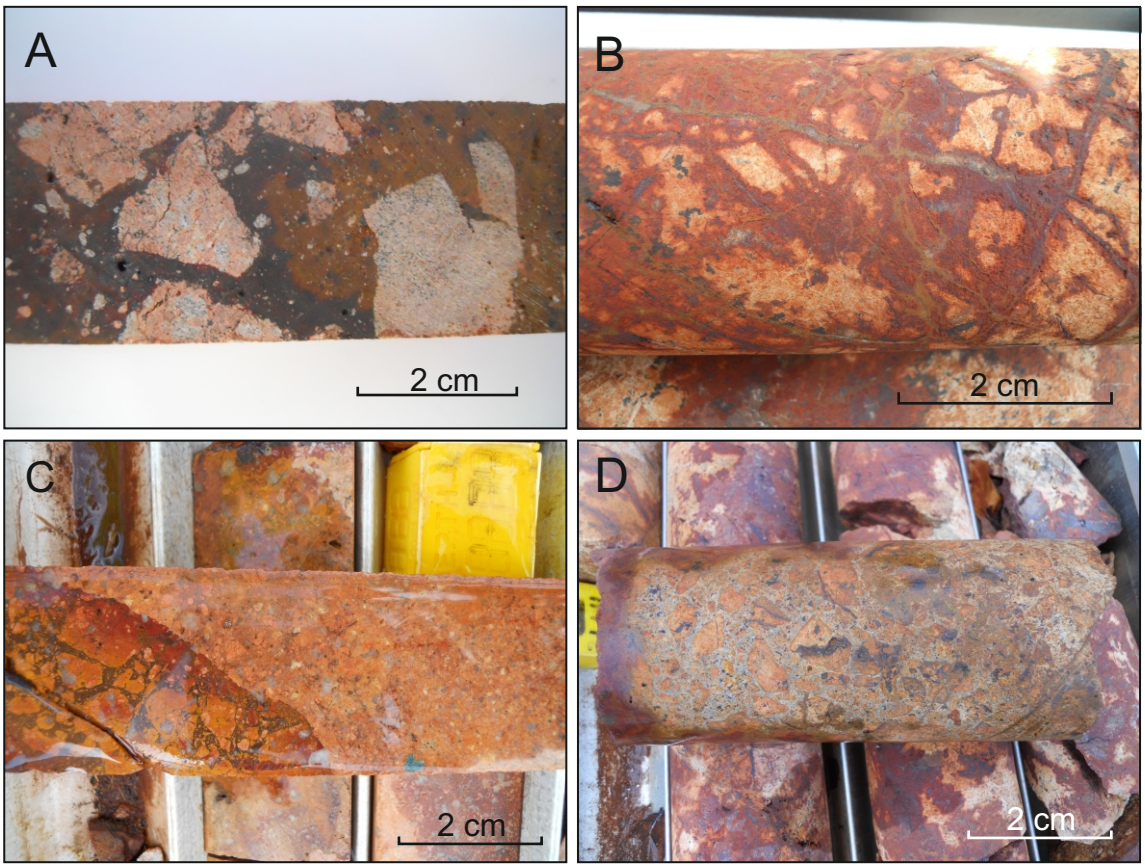

Fig. 7. Typical breccia types at Kitumba. A) Siderite-cemented syenite breccia. B) Crackle brecciation produced by hematite stockwork veins with late fracture-hosted chalcocite in a quartz porphyry protolith. C) Hematized and potassically altered quartz-porphyry rock in sharp contact with angular breccia. D) Mosaic breccia with clasts showing transition from early hematite (dark brown in the clasts) to K-alteration in sericitic groundmass. Drillcores S36_1 and S36_33.

SINGLE-COLUMN IMAGE

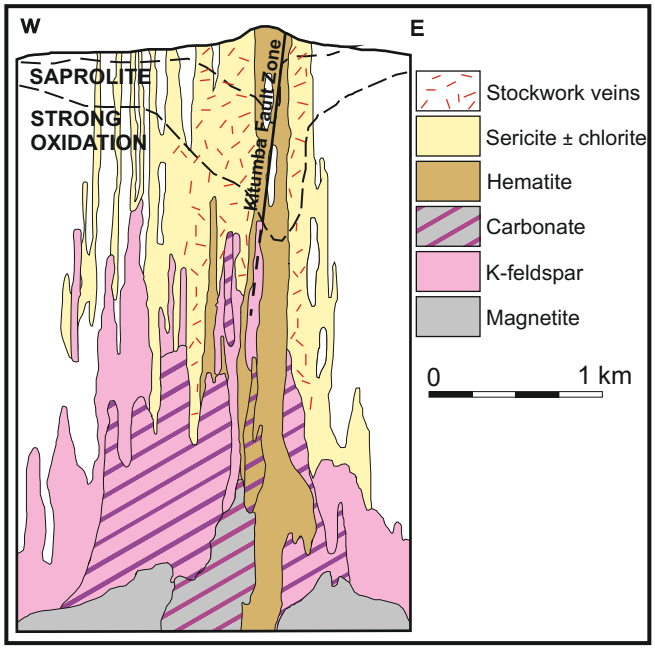

Fig. 8. EW-striking cross-section portraying the schematic interpretation of alteration zoning at Kitumba (modifie
Robertson, 2013, and references therein).

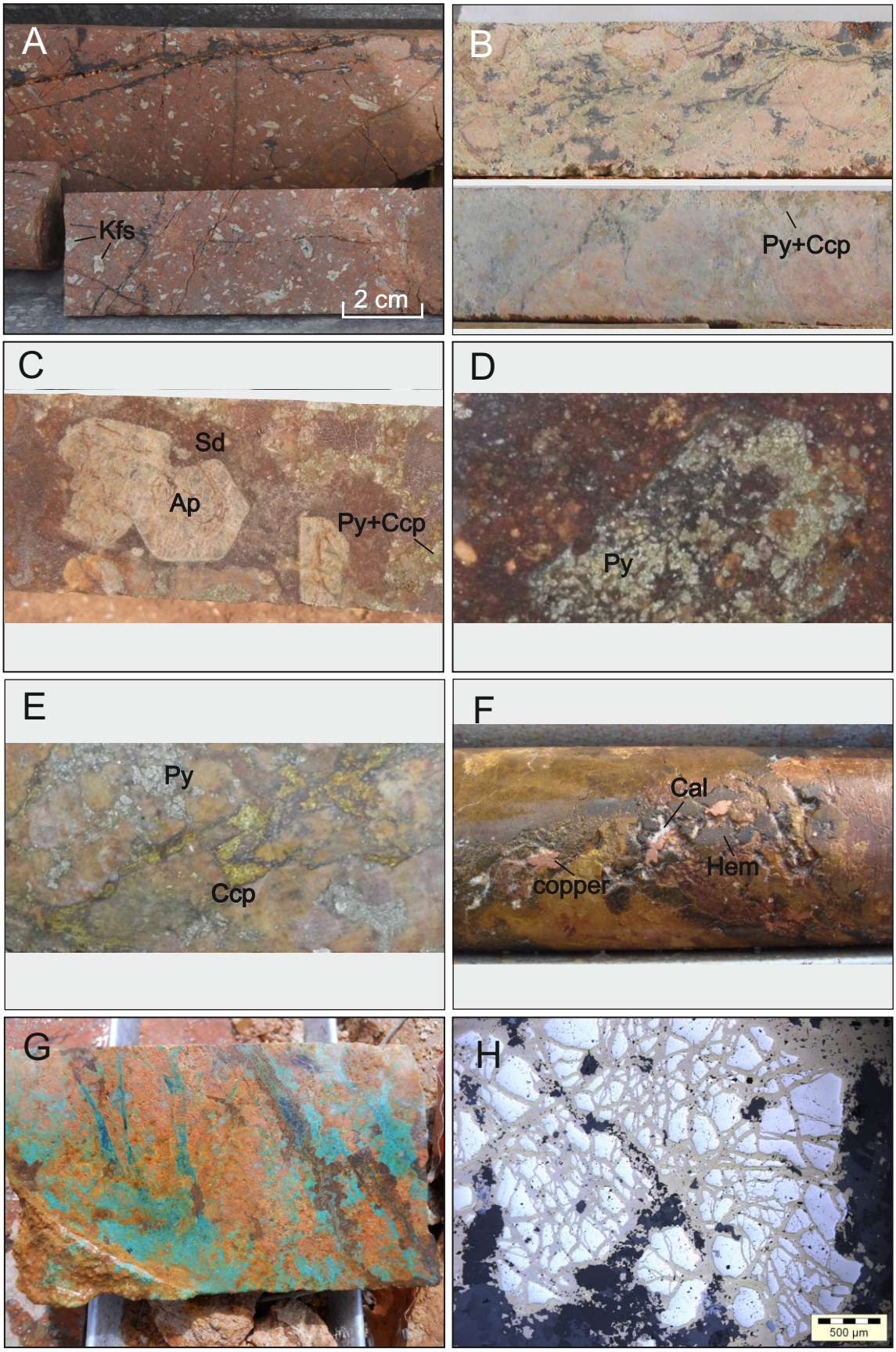

Fig. 9. Kitumba prospect lithologies and mineralization: A) Relatively low-altered feldspar porphyritic syenite with a salmon pink, hematite-dusted microcrystalline K-feldspar groundmass. Incipient sericitization of feldspar phenocrysts is apparent (drillcore S1_1). B) Texturally destructive sericite-hematite-carbonate hypogene alteration in syenite breccia. Interstices are filled with hematite-siderite ± quartz ± sulphide (drillcore S36_33). C) Apatite-carbonate-siderite vein. Siderite domains show interstitial pyrite rimmed by chalcopyrite (drillcore KITDD_34). D) Pyrite mineralized clast in hematized syenite breccia (drillcore S36_1, Waller et al., 2014). E) Fracture-filled pyrite and chalcopyrite in altered syenite (drillcore S36_33, Waller et al., 2014). F) Native copper, hematite and calcite in hematite breccia (drillcore S36_15). G) Supergene malachite and chrysocolla mineralization, extending down to 700 m depth (drillcore S36_1). H) Reflected light microphotograph of late, supergene chalcopyrite infilling cracks and partially replacing pyrite mineralization (drillcore S36_33). Ap = apatite; Cal = calcite; Ccp = chalcopyrite; Hem = hematite; Kfs = K-feldspar; Py = pyrite; Sd = siderite.

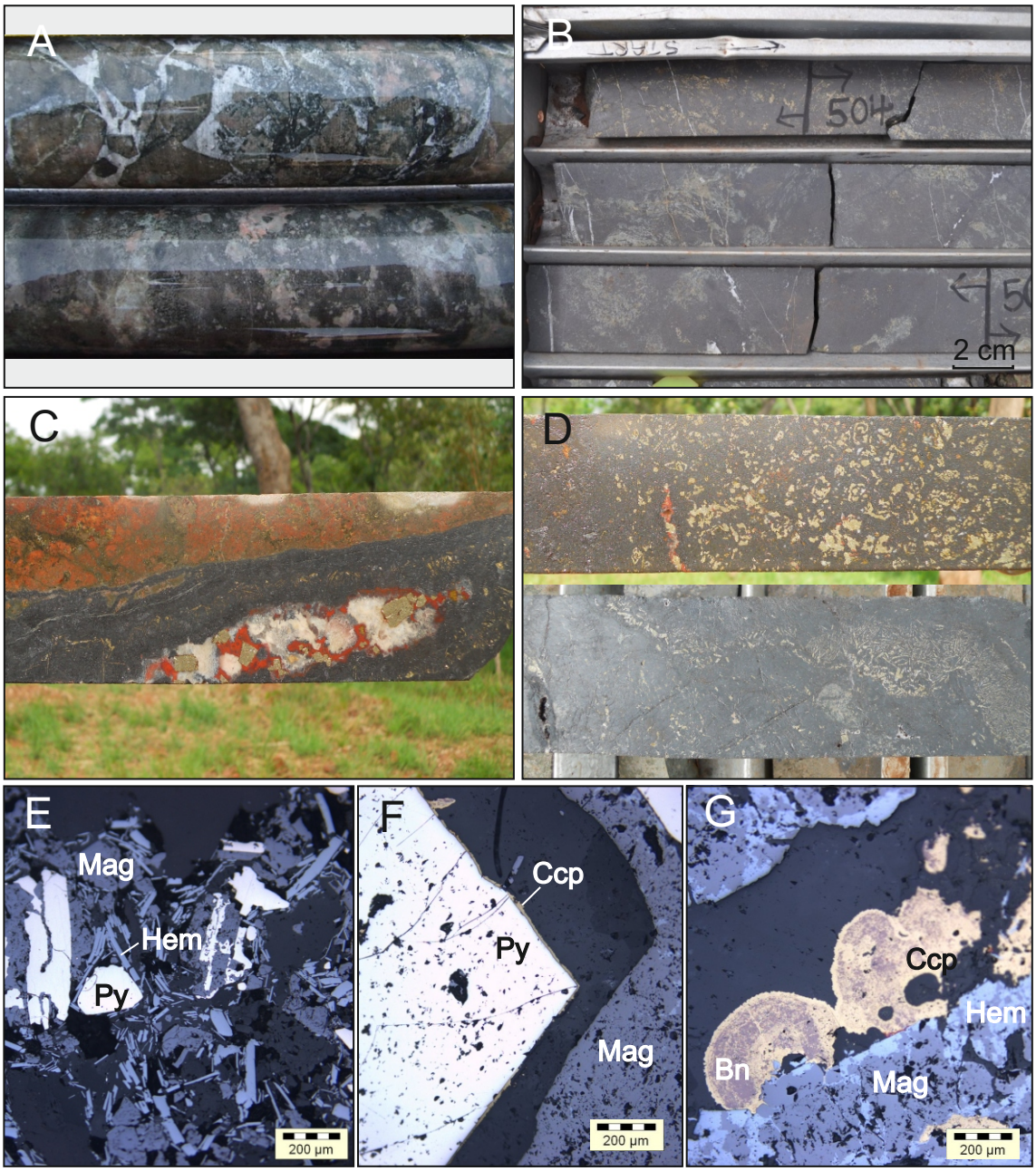

Fig. 10. Mutoya centre lithologies and mineralization. Mutoya s.s.: A) Magnetite-amphibole-apatite alteration in metasedimentary protolith (drillcore S30_1). B) Massive magnetite replacement partially mineralized with sulphides in disseminations and blebs (pyrite and minor chalcopyrite; drillcore MUM4D). Mushingashi: C) Cm-wide magnetite vein hosting pyrite and (minor) chalcopyrite with late stage mineralized quartz + calcite + siderite. D) Pyrite in orbicular, feathery, disseminated textures in massive magnetite. E) Reflected light microphoto: hypogene magnetite (dark blue) and pyrite crystallization, followed in time by specularite grown as needles (light bluish-gray). F) Reflected light microphoto: thin chalcopyrite rims growing on euhedral pyrite. G) Reflected light microphoto: hematite (light bluish-gray) overprinting magnetite (dark blue). Botryoidal chalcopyrite aggregates (yellow) replaced by late bornite (pink). Mushingashi samples from drillcore MUM6BD. Bn = bornite; Ccp = chalcopyrite; Hem = hematite; Mag = magnetite; Py = pyrite.

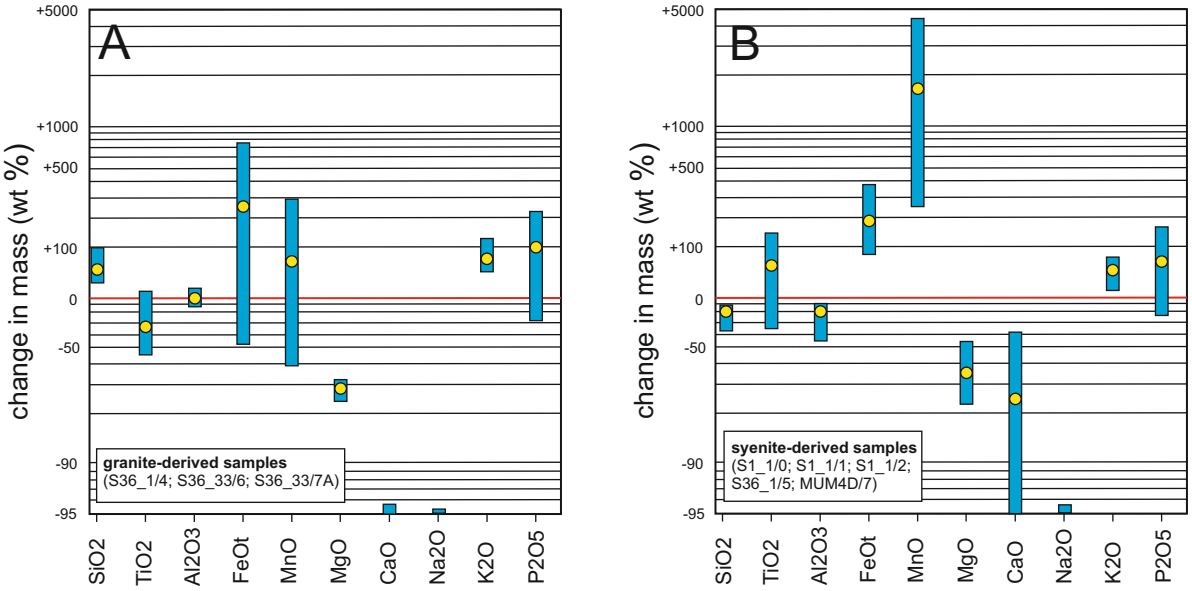

Fig. 11. Ranges (light blue bars) and averages (yellow dots) of mass changes (in wt %) for major elements in altered syenites (A) and granites (B) ofthe analyzed cores, according to the isocon method. Inferred protoliths: granite Z119A and syenite Z48. Immobile elements during evaluation of mass and chemical changes during alteration: Hf, Ta, Zr (syenite-derived samples); Al_2O_3, Ga, Y (granite-derived samples).

SINGLE-COLUMN IMAGE

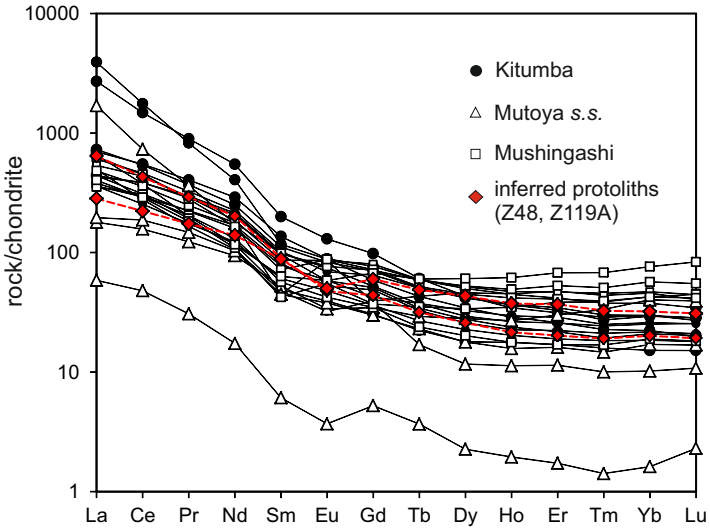

Fig. 12. Chondrite-normalized REE distribution of altered igneous rocks from the Mumbwa cores samples. Inferred precursor patterns (syenite Z48 and granite Z119A) are reported as red dashed lines (chondrite values after Boynton, 1985).

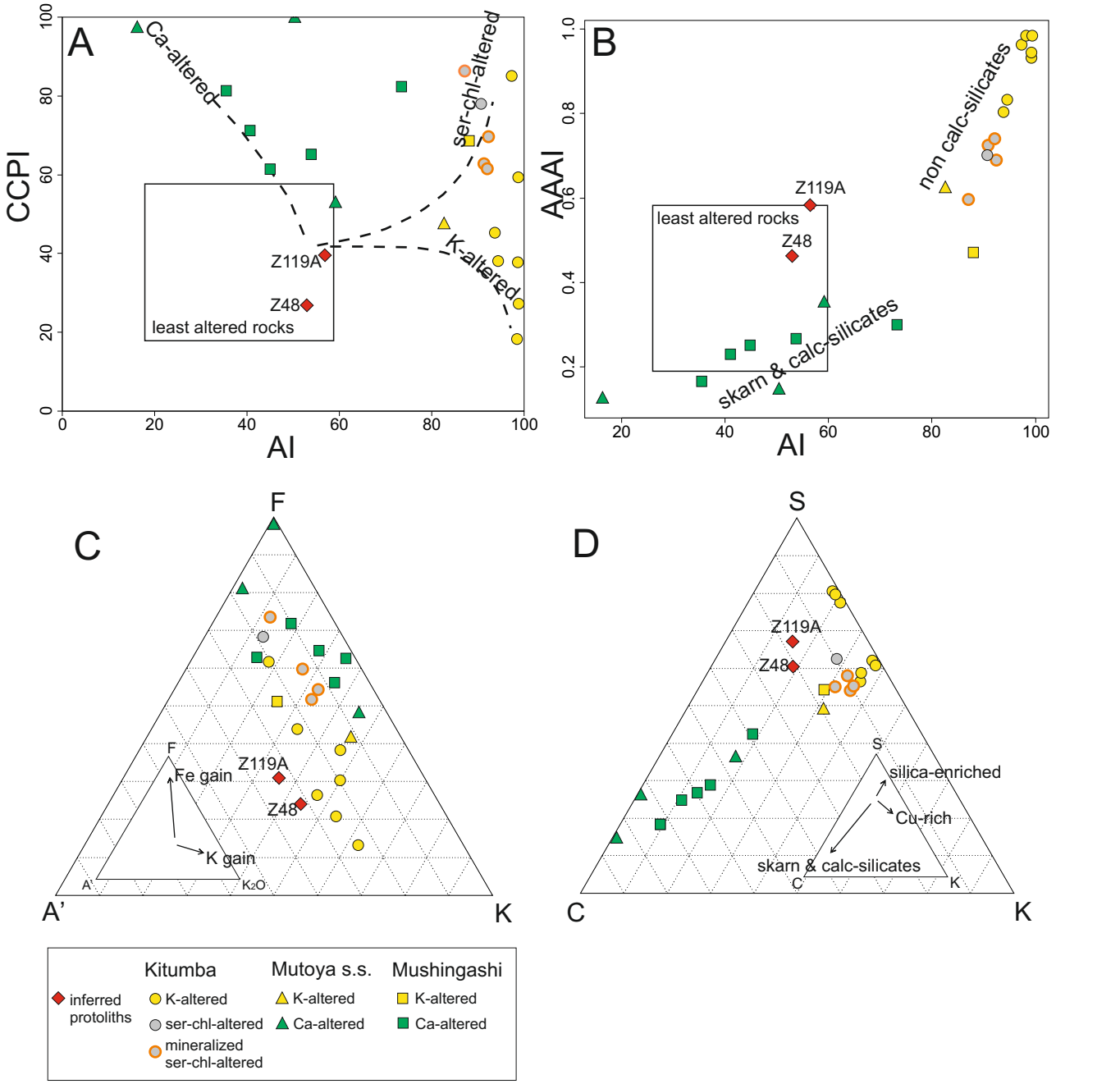

Fig. 13. Alteration boxes and ternary diagrams for analyzed samples displaying chemical mobility and alteration and mineralization vectors (see text). Sample provenance: circle = Kitumba prospect (Sugar Loaf centre); triangle = Mutoya s.s. prospect; square = Mushingashi prospect (Mutoya centre). Red diamonds: inferred protoliths. Alteration: yellow symbols = potassic alteration; grey symbols = sericite-chlorite alteration; green symbols = Ca-alteration. The 4 sericite-chlorite-rich high-Cu mineralized samples from Kitumba are represented as heavy orange contour circles. A) CCPI vs. Al diagram (after Large et al., 2001) discriminating between the main alteration styles; CCPI (chlorite-carbonate-pyrite index) = 100 x [(MgO+FeO)/(MgO+FeO+Na_2O+K_2O)]; Al (Ishikawa alteration index, after Ishikawa et al., 1976) = 100 x [(K_2O+MgO)/(K_2O+MgO+Na_2O+CaO)]. B) AAAI vs. Al diagram showing distinct paths followed by Ca-rich and Ca-poor rocks. AAAI (advanced argillic alteration index, after Wiliams and Davidson, 2004) = 100 x SiO_2/[SiO_2+(10 x MgO)+(10 x CaO)+(10 x Na_2O)]. The boxes in both diagrams represent the inferred field for unaltered rocks (after Wiliams and Davidson, 2004; Bonnet et al., 2005). C) A'FK diagram indicating Fe- or K-gain. A'=Al_2O_3+Fe_2O_3-(K_2O+Na_2O+CaO); F=(FeO+MnO+MgO); K=K_2O; see also Bonnet and Corriveau (2007). D) CKS (C=Ca x 3; S= SiO_2; K=K_2O) diagram showing silicification and Ca-enriched paths, as well as trends for Cu-mineralized rocks.